Additive Manufacturing 88 (2024) 104267

Contents lists available at ScienceDirect

Additive Manufacturing

journal homepage: www.elsevier.com/locate/addma

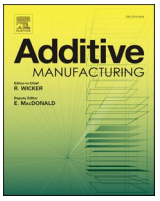

The influence of microstructural heterogeneities on high-temperature mechanical properties of additively manufactured γ'-forming Ni-based alloys

Venkatesh Pandian Narayana Samy [a,*], Frederike Brasche [a], Ivo Šulák [b], Bhupesh Verma [c], Benedikt Nowak [d], Zdeněk Chlup [b], Tomáš Záležák [b], Johannes Henrich Schleifenbaum [c], Ulrich Krupp [a], Christian Haase [a,e]

[a] RWTH Aachen University, Steel Institute, Chair Materials Engineering of Metals, Intzestraße 1, Aachen 52072, Germany
[b] Institute of Physics of Materials, Czech Academy of Sciences, Žižkova 22, Brno 616 00, Czech Republic
[c] RWTH Aachen University, Digital Additive Production, Campus-Boulevard 73, Aachen 52074, Germany
[d] VDM Metals International GmbH, Research and Development Department, Kleffstraße 23, Altena 58762, Germany
[e] Technical University Berlin, Chair Materials for Additive Manufacturing, Ernst-Reuter-Platz 1, Berlin 10587, Germany

ARTICLE INFO

Keywords:
Additive manufacturing
Ni-based alloys
Creep properties
TEM
SXRD
Heterogeneities

Abstract: Additive manufacturing (AM) of metallic materials yields distinctive hierarchical and heterogeneous microstructures owing to the complex thermal conditions during the build-up process. Consequently, the knowledge gained from creep properties of conventionally manufactured (CM) Ni-based alloys cannot be directly applied to AM-processed alloys. Furthermore, insufficient creep life has posed a significant challenge in the development of Ni-based superalloys fabricated by laser powder bed fusion (LPBF), one of the most important AM techniques. Nevertheless, limited research has been conducted to understand their creep behavior due to the time-consuming nature of creep testing and extended research cycles. This study delves into investigating the creep behavior of an additively manufactured, precipitation-strengthened Ni-based alloy (NiCrAl) in comparison to its CM counterpart, focusing on the structure-property relationships. Constant-load creep tests were conducted at temperatures of 750 °C and 950 °C up to a maximum duration of nearly 1500 h. Although both the AM and CM states demonstrated high creep activation energy and creep exponents, indicative of a dislocation climb mechanism, the AM state demonstrated inferior creep life and ductility compared to the CM state for creep times below 500 h. To gain deeper insights into the underlying mechanisms, multi-scale microstructural characterization was performed to understand the effect of the AM-inherent microstructure. Overall, this study provides a comprehensive understanding of the creep behavior of Alloy 699XA after AM and CM processes, emphasizing the significance of AM-specific microstructural heterogeneities.

1. Introduction

Ni-based alloys are widely used in high-performance components across various industries such as aerospace, petrochemical, and power generation owing to their exceptional mechanical properties including strength, corrosion resistance, and creep resistance. However, conventional manufacturing (CM) techniques, such as investment casting, pose challenges in producing high-performance and high-temperature Ni-based alloys due to work hardening and γ' precipitation during processing leading to expensive post-processing requirements to achieve target mechanical properties [1]. Additive manufacturing (AM) offers an alternative solution that not only enables net-shape production but also suppresses γ' precipitation due to the high cooling rate, making it a viable method for processing Ni-based alloys [1]. Nevertheless, the limited selection of commercially available alloys for AM necessitates the assessment of novel alloy compositions to optimize production and to enhance the overall performance of AM components [2]. Despite extensive research on LPBF of common Ni-based superalloys, such as alloy 625 [3] and alloy 718 [4], as well as CM247LC, alloy 738, and alloy X, there is a lack of studies on high-Cr (>25 wt%) Ni-based alloys [5–8]. Most of the investigated superalloys have a lower Cr content (~ 20 wt%) to prevent the precipitation of detrimental Cr-rich phases, e.g. α

* Corresponding author.
E-mail address: vnrayana@iehk.rwth-aachen.de (V.P. Narayana Samy).

https://doi.org/10.1016/j.addma.2024.104267
Received 19 February 2024; Received in revised form 6 June 2024; Accepted 16 June 2024
Available online 17 June 2024
2214-8604/© 2024 The Author(s). Published by Elsevier B.V. This is an open access article under the CC BY license (http://creativecommons.org/licenses/by/4.0/).

phase and σ phase that leads to embrittlement [9,10].

High-Cr Ni-based alloys, such as Alloy 690 (30 wt% Cr), are renowned for their excellent resistance to hot corrosion, stress corrosion cracking, and corrosion fatigue in aqueous environments [11–13]. However, traditional techniques, like casting and forging, encounter challenges in manufacturing these alloys due to the deterioration of thermoplasticity during the forging process, leading to cracking and reduced efficiency [14–16]. Laser metal deposition (LMD) of alloy K648, a high-Cr Ni-based alloy (32–35 wt% Cr), had shown the presence of detrimental α-Cr phases, resulting in reduced oxidation resistance (due to the low Cr content in the alloy matrix) [17]. Similarly, LPBF of alloy GH648, another high-Cr Ni-based alloy, results in unavoidable α-Cr phases and a lack of γ' phase, attributed to the enrichment of Ti and Al in the α-Cr phases [6,7] . Consequently, processing high-Cr Ni-based alloys through LPBF without the formation of α-Cr phase or TCP phases remains a challenge. Hence, this study focuses on AM of Alloy 699XA (NiCrAl), a novel high-Cr, precipitation-strengthened Ni-based alloy that is characterized by excellent metal dusting resistance [18–20].

Heterogeneity and anisotropy in as-built AM structures remains a limiting factor for widespread adoption and extensive use of AM [21, 22]. The unique thermal conditions (thermal gradients, thermal cycles, cooling rates) in the process lead to AM-specific heterogeneity in the microstructural features [23], grain morphology [24], and phase characteristics [25]. Furthermore, the mechanical properties of the AM Ni-based alloys are strongly influenced by these microstructure heterogeneities. Previous studies suggested that AM Ni-based alloys exhibit inferior creep behavior compared to their CM counterparts due to anisotropy [26], the presence of inter-metallic phases [27] and accelerated cavity nucleation kinetics [28–30], resulting from rapid solidification during LPBF as well as pronounced segregation [31] and the formation of fine-grained structures [25]. Davies et al. [36] observed that cast C-263 alloy displayed better creep resistance than AM C-263 due to a higher volume fraction of grain-boundary carbides. Kunze et al. [26] reported inferior creep properties of AM alloy 738LC compared to the cast alloy due to smaller grain size correlated to a higher fraction of more finely dispersed carbides in the LPBF-processed material. Furthermore, AM-specific heterogeneities have a significant influence on creep fracture modes. Sun et al. [25] reported the observations on an AM-fabricated Co-Cr-Mo alloy, which exhibited a combination of fine-grained and coarse-grained microstructures. During creep testing, fracture predominantly occurred in the fine-grain region, displaying an intergranular fracture mode. Adomako et al. [21] summarized the influence of heterogeneities on the mechanical characteristics of AM Ni-based alloys, highlighting the limited research on their impact on creep behavior. Therefore, it is essential to gain a thorough understanding of the underlying mechanisms linked to the heterogeneous microstructures introduced through the AM process.

Among the various mechanical properties of metals, creep resistance acts as the critical indicator of the component's performance at high temperatures and stresses. The creep performance and high-temperature properties of LPBF-produced Ni-based alloys are crucial for the lifetime of components in service. However, due to time-consuming experiments and long research cycles, there is limited literature on the creep properties of LPBF-processed Ni-based alloys [32]. Creep behavior has been investigated for LPBF-processed, common superalloys such as alloy 625 [33], alloy 718 [27], alloy 738LC [26,34], CM247LC [35], C-263 [36, 37] and alloy X [38]. While creep behavior has been studied in conventional manufacturing of single-crystalline γ'-strengthened Ni-based alloys [39–41], for γ'-strengthened polycrystalline materials, the focus has primarily been on dislocation activity and interaction with γ' precipitates, lacking consideration of grain microstructures or heterogeneities in AM [42,43]. Despite the critical importance of understanding creep behavior in additively manufactured Ni-based alloys, research is limited in this specific area [32] and there are no studies focusing on the creep properties of high-Cr Ni-based alloys manufactured by AM.

Thus, the literature review highlights the imperative need for a comprehensive investigation of the high-temperature properties of high-Cr Ni-based alloys processed by LPBF, especially considering the alloy's extensive application in petrochemical industries at service temperatures >500°C. Henceforth, the present investigation endeavors to scrutinize the underlying physical mechanisms governing the high-temperature behavior, the failure mechanisms and the corresponding structure-property correlations in Alloy 699XA. In this regard, various characterization techniques, including scanning electron microscopy (SEM) with electron backscatter diffraction (EBSD), scanning transmission electron microscopy (STEM), synchrotron X-ray diffraction (SXRD), as well as creep and tensile experiments were applied to examine the precipitation of carbides as well as γ' and to examine the microstructure evolution and the associated creep behavior and cavity formation. Specifically, this study thoroughly investigates the impact of heterogeneities resulting from the AM process in NiCrAl alloy after solution heat treatment (SHT) on creep properties and compares it with the CM counterpart (referred to as 'AM state' and 'CM state' respectively).

2. Applied methods

2.1. Material and processing

Initially, VDM Alloy 699XA was melted in an electric furnace and electro-slag remelted (ESR). Furthermore, the plates were fabricated via hot rolling, followed by solution heat treatment (SHT) and subsequent descaling by mill grinding. The plate material underwent subsequent preparation for tensile and creep testing and microscopic analysis.

The AM powder was produced using vacuum inert gas atomization (VIGA) with Ar gas. The nominal composition of the powder is given in Table 1. The resulting powder had a particle size distribution of 15–53 μm. LPBF was carried out on an EOS M290 machine equipped with a 370 W fiber laser with a 100 μm spot size, operating in an Ar atmosphere with an oxygen level of less than 200 ppm. The process parameters were varied, and the densities were analyzed using optical microscopy (c.f. Fig. A.1(a)). Samples with the highest density of 99.57 % were produced using a laser power of 260 W, scan speed of 1100 mm/s, hatch distance of 110 μm, a preheating temperature of 80 °C and a layer thickness of 40 μm (c.f. Fig. A.1(b)). A scan strategy with a bi-directional scan vector and 67° rotation between consecutive layers was used for all builds, without considering the contours. Only minor fractions of gas pores were detected as defects in the samples. As the primary focus of this study was placed on the mechanical properties, the as-built AM state was also SHT at 1200 °C for 1 h. The printing parameters and heat treatment regime were kept identical for all specimens of the AM state.

2.2. Microstructural characterization

Sample preparation for microstructural characterization comprised mechanical grinding using SiC paper with grit sizes of 80, 180, 320, 600, and 1200 respectively. Subsequently, mechanical polishing was conducted with diamond suspensions of 6 μm and 1 μm. The final preparation step included electro-polishing in a 10 % solution of oxalic acid at a voltage of 1–2 V for 5–10 s at a temperature of 16 °C.

Microstructure characterization was performed using scanning electron microscopy (SEM) with a field emission gun (FEG) Tescan Lyra that was equipped with electron backscatter diffraction (EBSD) and energy-dispersive X-ray spectroscopy (EDX) detectors. Backscattered electron (BSE) imaging and EDX measurements were obtained using a voltage of 10 kV. EBSD analysis was carried out with a step size of 250 nm at 20 kV and 12–25 mm working distance, and the EBSD data were processed using the MTEX toolbox [44,45], in MATLAB®. High angle boundaries (HAGBs) were defined based on a misorientation angle of $\theta \geq 10°$, and twin boundaries were identified as those with a 60° <111> and 40° <110> misorientation, with a tolerance of ±2° based

Table 1
Nominal composition of NiCrAl alloy (Alloy 699XA, VDM Metals GmbH, Germany) [20].

	Ni	Cr	Al	Fe	Mn	Si	Ti	Nb	Cu	Zr	C	N	P	S	B
min	Bal.	26.0	1.9	-	-	-	-	-	-	-	0.005	-	-	-	-
max	Bal.	30.0	3.0	2.5	0.50	0.60	0.60	0.50	0.50	0.10	0.100	0.05	0.02	0.01	0.008

on the Brandon criterion [46]. Local misorientation was investigated using the kernel average misorientation (KAM) parameter, which was calculated at every EBSD measurement point as the average misorientation angle between the given measurement point and its neighbors. The definition of KAM at pixel i, based on it n nearest neighbors (j) is given as

$$KAM_i = \frac{1}{n} \sum_{j=1}^{n} \theta_{ij}$$

The KAM parameter is limited to quantifying short-range orientation misconsistency within a pixel and is not well-suited for differentiating between the grain-boundaries of recrystallized and parent grains. Therefore, grain orientation spread (GOS) was employed to measure the mean misorientation angles of a grain to quantify partial recrystallization [47,48]. For a grain numbered i, its GOS is defined as

$$GOS_i = \frac{1}{n_i} \overset{j}{\underset{j=1}{=}} \sum^{n_i} \omega\left(g_j, \quad < g_i >\right)$$

where n_i is the number pixels of the grain numbered i, j enumerates the pixels in the grain i and $\omega\left(g_j, < g_i >\right)$ is the misorientation angle between the pixel and grain i. In this study, GOS threshold values of 2.1 ° was defined to identify the recrystallized grains. Furthermore, the grain shape factor (F), defined as the grain boundary perimeter (P_{GB}) divided by the equivalent perimeter (P_E) was calculated using MTEX based on the EBSD data before and after creep for both the AM and CM states [49]. This calculation was performed to understand the grain evolution during creep.

$$F = \frac{P_{GB}}{P_E}$$

Transmission electron microscopy (TEM) measurements were conducted on thin TEM foils on both heat-treated AM and CM states prior and after high temperature experiments to investigate the dislocation-particle interactions, precipitation kinetics of γ' and formation of grain-boundary carbides. TEM foils were prepared from ground discs with the thickness of approximately 60–80 μm that were electrolytically thinned in Struers TenuPol-5 using a solution of 4.9 $HClO_4$ + 95.1 CH_3COOH at 8 °C. The analyses were taken using a JEOL JEM-2100 F and Talos™ F200i operated at 200 kV and equipped with bright-field and high-angle annular dark-field detectors for observation in the scanning mode. The analysis of the selected area electron diffraction (SAED) patterns was carried out using the JEMS software [50]. The γ' precipitates and carbides were analyzed with respect to their volume fraction, size, and inter-particle spacing using the image analysis software ImageJ [51].

The evolution of γ' in AM state was investigated during aging at 750°C for varying durations using synchrotron X-ray diffraction (SXRD) analysis. The diffraction patterns were captured using the PETRA III beamline P21.2 at DESY in Hamburg, with a wavelength of 0.15 Å, and were analyzed by integrating complete n rings between 2.8° to 16.6° for 2θ using Fit2D [52,53]. The peak-to-phase relationships, lattice parameters and phase fractions were determined using Rietveld refinement with the open-source software material analysis using diffraction (MAUD) [54].

2.3. Mechanical testing

The AM specimens for tensile and creep testing were extracted from a printed block along the transverse direction (c.f Fig. A.2(a)). Tensile tests were performed on both heat-treated AM and CM states using a Zwick/Roell Z50 screw-driven testing machine complying with ČSN EN ISO 6892 standard. The tests were conducted at various temperatures, including room temperature, 550°C, 750°C, 850°C, and 950°C, to investigate the temperature dependence of the tensile properties. Miniaturized M6 tensile specimens with a gauge length of 9 mm and a diameter at gauge length of 3 mm were used for the position-controlled tests with a loading speed of 1 mm/min (c.f Fig. A.2(b)). The specimens were heated at a rate of 20 °C/min, and the test temperature was allowed to stabilize for 20 min before conducting the tests.

Similarly, creep tests were performed on both heat-treated AM and CM states according to the ASTM E 139 standard. The tests at 750 °C were performed using self-designed creep devices [55], on flat dog-bone specimens (c.f Fig. A.2(c)). The machines have a lever construction that automatically adjusts the applied force, thus a constant stress was applied upon the specimen. The tests at 950 °C were conducted on Zwick/Roell Kappa LA screw-driven machine with a softening lever with the same dogbone-shaped specimens (c.f Fig. A.2(c)). Both the creep machines were equipped with a protective Ar atmosphere. During the tests, the temperature was held constant with a Eurotherm 2416 electronic regulation with a controlling Ni-Cr or Pt-Rh thermocouple placed in close proximity of the sample gauge length. The displacement was measured by a half-bridge induction coil sensor connected to a measuring amplifier. The induction sensor provided a measuring range of ± 5 mm or ± 10 mm.

3. Results

3.1. Powder characteristics

The AM state specimens were manufactured utilizing gas-atomized powders with particle sizes ranging from 15 μm to 53 μm, as shown in Fig. 1**a**. An assessment of the powder properties via mass spectrometry analysis revealed an oxygen content of 100 ppm, which was not present in CM specimens. The SEM (c.f Fig. 1**a**), EBSD (c.f Fig. 1**b**), bright-field TEM (c.f Fig. 1**c**) and TEM-EDX (c.f Fig. 1**d-h**) images demonstrate the powder characteristics. The powder particles had a polycrystalline, fully face-centered cubic (fcc), fine-grained structure without any detected segregation, carbides, or γ' in the analysis. The composition of the powder determined by EDX analysis is shown in Table 2.

3.2. Initial microstructure after SHT

SEM analysis and EDX mapping were performed on the annealed AM state, and the results are presented in Fig. 2**.** The SEM analysis (c.f Fig. 2**a**) revealed a recrystallized microstructure with equiaxed grains. The EDX analysis (c.f Fig. 2**b-e**) showed that the alloying elements were uniformly distributed after SHT, except for C and Cr, which were enriched at the grain-boundaries. Furthermore, the EDX point analysis (Table A.1 and Fig. A.6) indicated that grain-boundaries were slightly enriched with Al (2.35 wt%) and Cr (31.78 wt%) compared to the matrix with Al (2.09 wt%) and Cr (27.92 wt%). Notably, no grain-boundary carbides, such as $M_{23}C_6$, were observed in the initial microstructure.

The EBSD analysis conducted on AM state after the SHT revealed a

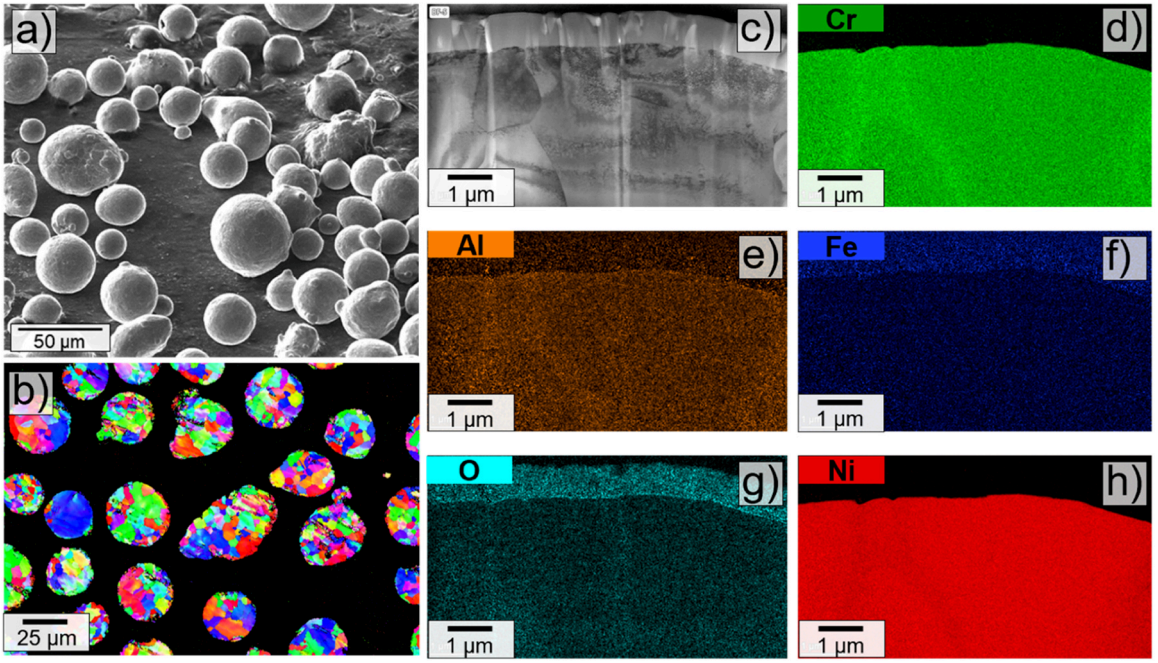

Fig. 1. Characterization of Alloy 699XA gas-atomized powder used for LPBF. (a) SE-Micrograph, (b) EBSD analysis showing the orientation maps, and (c-h) TEM analysis with EDX showing the (c) area selected and composition distribution of (d) Cr, (e) Al, (f) Fe, (g) O, and (h) Ni.

Table 2
The chemical composition of the gas-atomized AM state powder measured by EDX analysis.

Elements (wt%)	Ni	Al	Cr	Fe
powder – AM state	Bal.	2.3	29.1	0.1

homogeneous microstructure characterized by equiaxed austenitic grains, as depicted in Fig. 3. Notably, distinct features associated with the AM process, such as long columnar grains, melt pool lines, and pronounced crystallographic texture were eliminated due to static recrystallization. To identify local misorientations within the structure, KAM maps were employed to identify regions with increased misorientation, indicative of highly strained areas due to in-complete recrystallization. As seen in Fig. 3**b,** they revealed the presence of large grains with higher KAM values indicating non-recrystallized and strained regions. To furthermore differentiate the non-recrystallized grains, GOS maps were analyzed, as seen in Fig. 3**c**. Grains with a GOS value above 2.1° (green and yellow) were identified as grains with high mean misorientation and thus quantified as non-recrystallized grains. Furthermore, these grains exhibited a high density of geometrically necessary dislcocations (GND) as seen in Fig. 3**d** and did not contain annealing twins. Thus, the KAM, GOS, and GND maps clearly demonstrated that a complete recrystallization was not achieved for AM state after SHT.

EBSD results of CM state, heat-treated at 1200 °C for 1 h, are presented in Fig. 4**a-d** for a direct comparison. Unlike the AM state, the KAM (c.f Fig. 4**b**), GOS (c.f Fig. 4**c**) and GND (c.f Fig. 4**d**) analysis indicated complete recrystallization without any distinct heterogeneities. Grain size distributions were determined for both CM and AM state from EBSD analysis, excluding the twin boundaries, as shown in Fig. 4**e**. The results revealed an unimodal distribution, with an average grain size of 32 µm for the AM state and 60 µm for the CM state after SHT, excluding twins. Furthermore, the fraction of Σ3 and Σ9 grain-boundaries was analyzed in MTEX, as shown in Fig. 4 **f, g**. The total fraction of twins was lower for CM state compared to AM state.

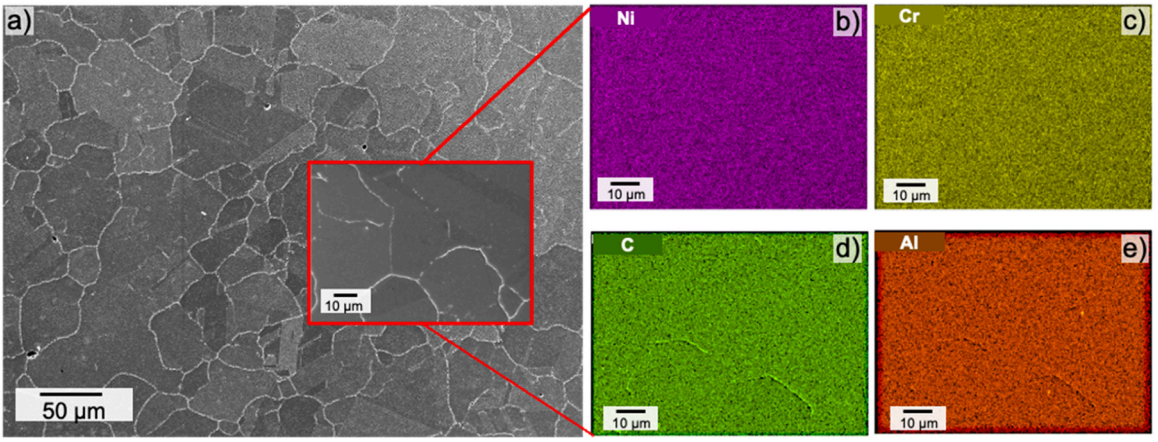

Fig. 2. SEM and EDX Analysis of the AM state. (a) SEM analysis of the SHT AM state with the inset showing the region measured for EDX area mapping. EDX area mapping showing the composition distribution of (b) Ni, (c) Cr, (d) C, and (e) Al.

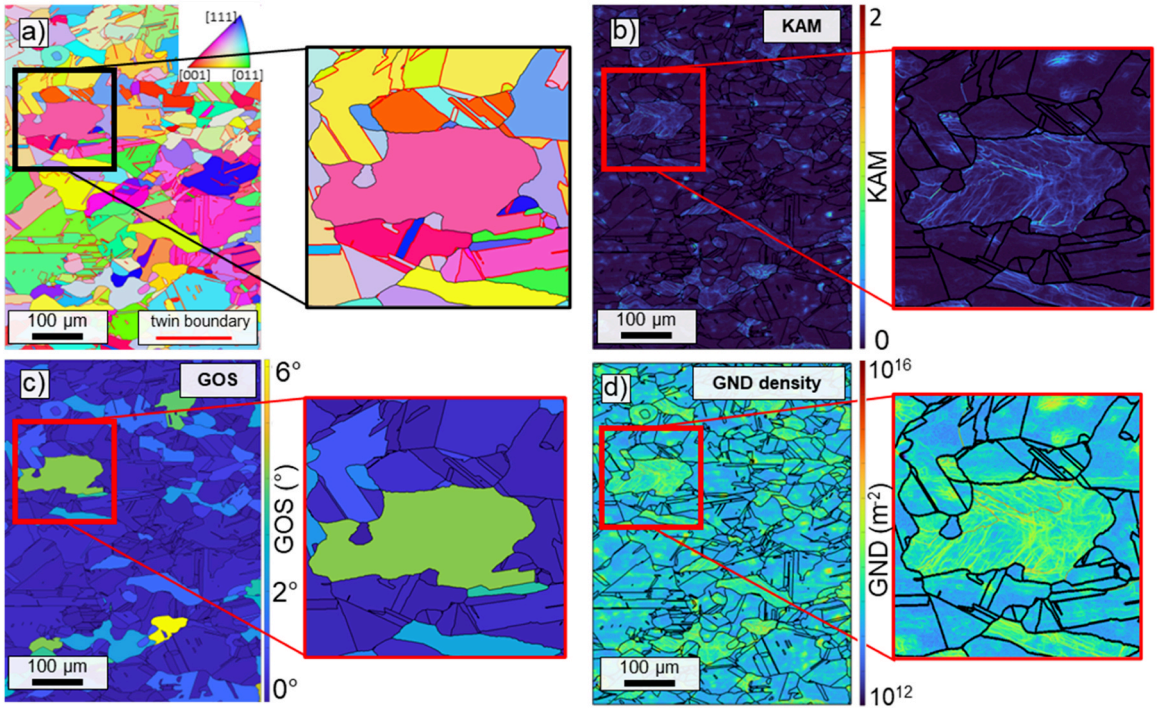

Fig. 3. EBSD analysis of the AM state after SHT. (a) IPF maps with red lines highlighting the twin boundaries (IPF color-coding taking the z-axis parallel to the build direction as reference axis), (b) KAM maps as contour with misorientation between 0°- 2° highlighting a region with high average misorientation, (c) GOS maps showing the overall in-grain misorientation, with a specific grain having a higher spread than threshold (2°) and (d) GND density map showing several grains with high dislocation density.

TEM analysis was conducted on the SHT AM and CM states, and the results are presented in Fig. 5. The particles were identified as intragranular $M_{23}C_6$ carbides and revealed a high concentration of Cr within the particles, as confirmed by EDX analysis (c.f Fig. 5**a, b**). The volume fraction, particle size, and number density of particles measured from several TEM micrographs are shown in Table 3**.** The AM alloy exhibited a higher dislocation density of 7.27 $\times 10^{13}$ (m^{-2}), whereas the CM alloy had a dislocation density of 2.66 $\times 10^{13}$ (m^{-2}) (c.f Fig. A.5), both measured by the method by Pesicka et al. [56]. Notably, no γ' precipitates were observed in TEM. Furthermore, TEM analysis revealed the presence of significant parallel dislocation arrays or loops in the samples interacting with the carbides, as illustrated in Fig. 5**c** and 5**f.**

The TEM analysis furthermore revealed the clustering of ZrN and Al_2O_3 particles, as shown in Fig. 6. These clusters were formed through the nucleation of ZrN on the corundum particles early in the solidification processes. This preferential precipitation of ZrN on the oxide rather than in the liquid has been observed and this relationship between oxides and nitrides has been shown for several steels during solidification [57,58]. The formation of Al_2O_3 particles was attributed to the contamination of powders with oxygen, as confirmed by mass spectrometry analysis of the powders, which has been reported previously in AM-processed Ni-based alloys [59–61]. No ZrN and Al_2O_3 particles were observed in the CM state.

Alloy 699XA has been meticulously tailored for demanding applications in high-pressure and high-temperature settings within the petrochemical industries, boasting remarkable resistance to metal dusting. In the realm of additive manufacturing, Alloy 699XA exhibited exceptional printability, devoid of solidification cracks and the undesirable α-Cr phase. The alloy contains roughly 0.02 wt% of Zr, employed in addition to bolster its resistance to creep deformation. However, the presence of Zr has posed challenges in AM processing, as it tends to partition into the last solidified liquid, resulting in the formation of low melting films rich in Zr, ultimately leading to the formation of hot cracks [62,63]. However, in the case of AM state, the formation of ZrN particles (c.f Fig. 6) enabled the encapsulation of Zr within the particle, averting its pronounced segregation in the interdendritic regions. Furthermore, despite zirconia having a higher energy of formation (ΔG_f°) in comparison to Al_2O_3, only Al_2O_3 was formed. This was attributed to the alloy's higher Al content, which readily facilitated the formation of Al_2O_3. Furthermore, unlike LMD of K648, a high-Cr Ni-based alloy, where the undesirable α-Cr phase was observed, it was conspicuously absent in the AM state [17]. Rapid cooling rates during LPBF compared to LMD prevented the formation of the α-Cr phase and ensured the Cr was available completely in the matrix as inferred from the Scheil and equilibrium simulations [64], thus enhancing oxidation resistance.

3.3. Tensile properties

Fig. 7 presents the engineering stress-strain curves of the CM and AM states tested at various temperatures. The corresponding 0.2 % offset yield strength (YS), total elongation (∈) and ultimate tensile strength (UTS) are shown in Fig. 7**b**. The graph reveals that both AM and CM materials exhibited serrated flow behavior at temperatures of 550°C and 750°C. The tensile properties of AM and CM states were comparable up to temperatures of 750°C (c.f Fig. 7**a** and 7**b**). However, at temperatures above 750°C, the AM state displayed poor elongation-to-rupture.

To comprehend the failure mechanisms of AM state specimens, their fracture surfaces were analyzed, as illustrated in Fig. 8**.** The fractography image of the specimen deformed at room temperature and 550 °C showed dimples and revealed a fully ductile fracture mode (c.f Fig. 8**a** and Fig. 8**b**). The drop in ductility of CM and AM state at 750°C is supported by the fractography image given in Fig. 8**c**, which exhibited a ductile-brittle mixed failure mode. The low elongation characteristic of AM state at 850°C and 950°C was supported by the fractography images given in Fig. 8**d** and Fig. 8**e,** revealing intergranular fracture. The AM material behaved uniformly up to 850 °C but underwent a change beyond this temperature, possibly influenced by the presence of Al_2O_3 oxides. Though the existence of the oxides has a positive effect on the

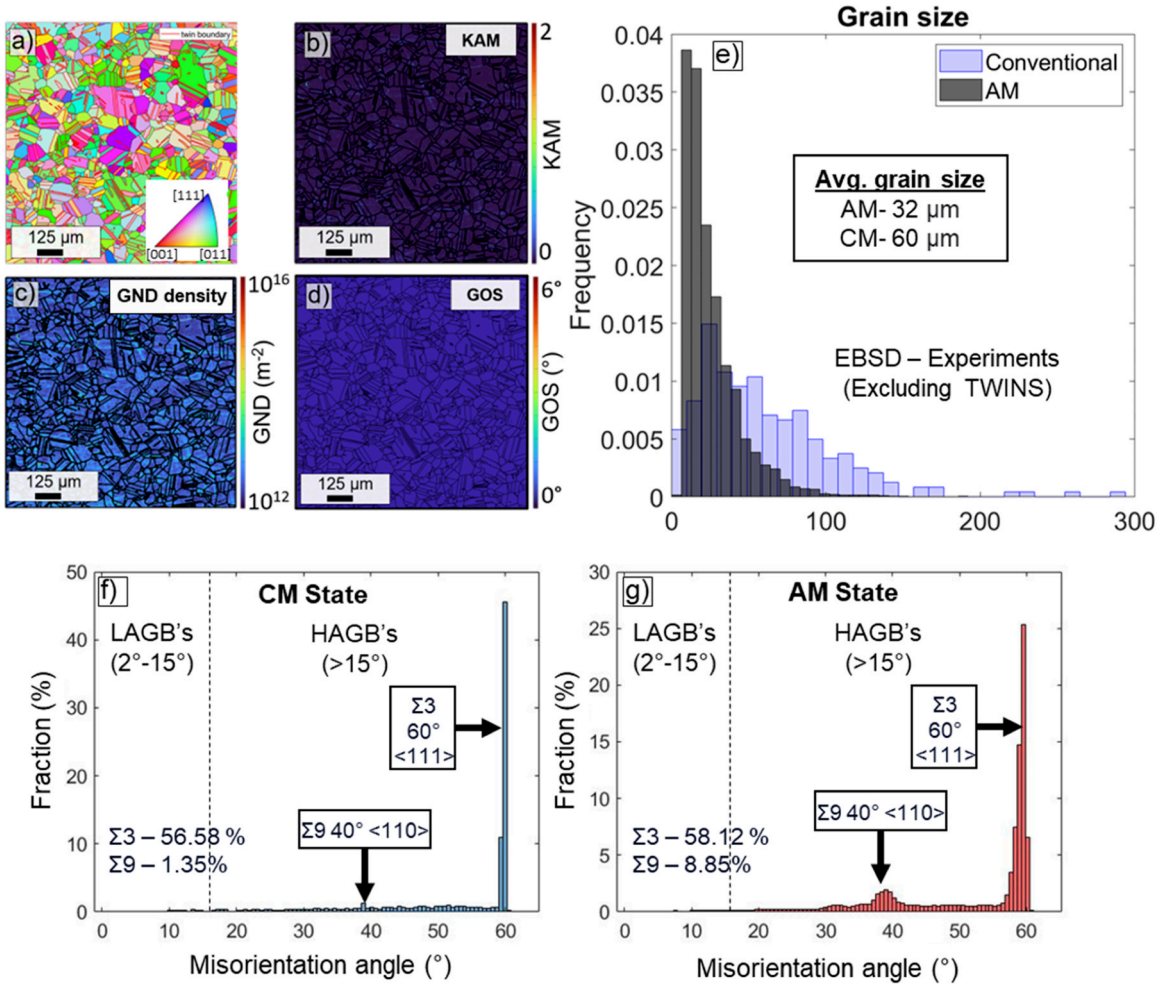

Fig. 4. EBSD analysis of the solution-annealed CM state after SHT. (a) IPF map with red lines highlighting the twin boundaries (IPF color-coding taking the z-axis parallel to the build direction as reference axis), (b) KAM map as contour with misorientation between 0°- 2°, (c) GND density map, (d) GOS map showing the overall misorientation, and (e) grain size distribution excluding the twin boundaries for the AM and CM states after SHT and the corresponding average sizes. Grain misorientation angle distribution for (f) CM and (g) AM state after SHT from EBSD analysis showing Σ3 and Σ9 grain-boundaries, low-angle boundaries (LAGB) and general high-angle boundaries (HAGB).

strength of the sample, due to their large size, in the AM state they lead to weakening of grain boundaries. Additionally, the oxides act as crack initiation sources, affecting the plasticity of the sample and leading to intergranular fracture of the alloy [65,66]. Above 850 °C, the CM material became more ductile due to transcrystalline fracture (c.f Fig. 8**f**).

3.4. Creep properties

Creep testing of the AM and CM states were conducted at temperatures of 750 °C and 950 °C, as presented in Fig. 9. The graphs show the creep strain as a function of time for both alloys at 750 °C (c.f Fig. 9**a**), and the creep strain rate as a function of time for AM (c.f Fig. 9**b**) and CM state (c.f Fig. 9**c**) at both 750 °C and 950 °C (c.f Fig. 9**d-f**). To measure the activation energy, creep tests were carried out at 150 MPa at 700 °C and 800 °C for both AM and CM states (c.f Fig. 9**g-h**). The creep curves for both alloys at 750 °C and 100 MPa exhibited a distinct primary creep regime, followed by a steady-state secondary creep stage, and finally, a rapid rise of the creep rate during the tertiary creep stage. However, the steady-state creep partially overlaps with the tertiary creep state for most of the tests, as the strain rate gradually increases quickly after reaching the minimum value. For higher applied stresses, the steady-state creep stage is considerably longer with respect to the overall duration of the test as well the overall true strain. The AM alloy demonstrated a creep strain rate slightly lower than that of the CM alloy at 750 °C and higher at 950 °C. Furthermore, the former exhibited poor ductility and a shorter lifespan, as seen from the significantly shorter tertiary creep regime. The distinctive features in the creep behavior between AM and CM states at 750 °C were as follows: the AM alloy had (1) an accelerated creep failure, (2) lower ductility and (3) lower or comparable minimum strain rate. However, at 100 MPa, AM samples performed better than CM state. As the temperature increased to 950 °C, the properties of the AM state deteriorated further.

Fig. 10**a** and Fig. 10**b** show a plot of minimum strain rate and stress, indicating a power law creep behavior for the AM and CM states with high stress exponents and high activation energy at 750 °C and 950 °C. Furthermore, the creep behavior of the AM and CM states was analyzed using the Monkmann-Grant relationship [67] and Larson-Miller parameter relationship [68]. In these methods, the relationship between the minimum creep rate ($\dot{\varepsilon}_m$) and applied stress(σ) to the time to fracture (t_f) were analyzed, according to the Monkmann-Grant relationship,

$$t_f \quad (\dot{\varepsilon}_m)^m = \quad C_{MG}$$

where C_{MG} and m are constants. The Monkman-Grant plot for the AM and CM states is shown in Fig. 10c. A linear relationship between the AM and CM states was observed, indicating the creep rupture was deformation controlled [69]. Furthermore, according to the Larson-Miller

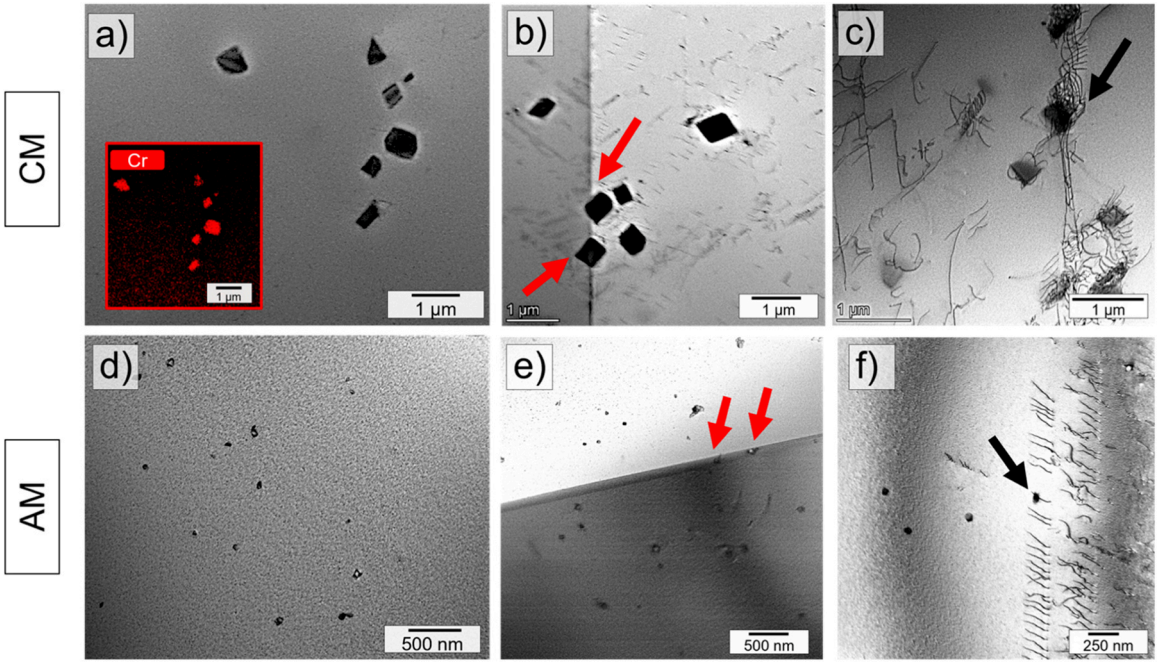

Fig. 5. TEM analysis of the SHT AM and CM alloy. Carbides within the matrix and carbides along the grain-boundaries for (a, b) CM alloy with TEM-EDX area analysis in the inset of (a) showing Cr enrichment in the particles and (d, e) AM state. The red arrows indicate carbides situated at a grain-boundary. Carbides and dislocation interaction is highlighted by black arrows in the (c) CM and (f) AM state.

Table 3
Characteristics of $M_{23}C_6$ measured observed in AM and CM alloys after SHT.

Alloy	Volume fraction (%)	Average particle size (nm)	Particle number density (x 10^{12} m^{-2})
AM	0.53	68	1.15
CM	1.8	466	0.14

parameter (LMP),

$$LMP = T(C + \log t_f)$$

where C is a constant and T is the temperature. Experimental data were constructed and fitted to a log-log plot of t_f and $\dot{\epsilon}_m$, as shown in the Fig. 10**c**. The AM state exhibited a poor creep life compared to the CM state, as seen from the Larson-Miller plot at 750 °C. The constants used in the Monkmann-Grant relationship and LMP are specific to the defined rate-controlling mechanism and cannot be extrapolated to other creep regimes [70].

To understand the failure mechanisms, representative fracture surfaces of specimens subjected to creep tests at 750 °C and 950 °C are shown in Fig. 11. In both cases, the fracture surfaces exhibited cavities, wedge cracks, extensive dissection, and fracture occurred predominantly along grain-boundaries.

3.5. Microstructure evolution at elevated temperature

Alloy 699XA exhibited the formation of intergranular $M_{23}C_6$ carbides as well as the γ' phase that controlled directly the thermo-mechanical behavior. The elemental analysis of the AM 100 MPa creep-fractured sample identified the phases as $M_{23}C_6$ carbides, which are enriched in Cr (c.f Fig. 12 **a-f**). The precipitation of $M_{23}C_6$ carbides in both AM and CM states was observed exclusively at high-angle grain boundaries (c.f Fig. 12 **g-j**), without occurrence at twin boundaries, due to the low grain-boundary energy of twin boundaries [71]. There was a significant difference in the evolution of carbides between AM and CM states. The AM state exhibited the formation of uniform fine carbides consistently distributed along the grain boundaries (c.f Fig. 12**a**, **h** and **j**). Conversely, the CM state displayed the formation of coarse, granular, and discrete carbides along the grain boundaries (c.f Fig. 12**g** and **i**).

Following STEM analysis of AM and CM states aged at various time intervals and creep-tested at 750 °C, the precipitation of the γ' phase was observed. No discernible difference in γ'-precipitation behavior was observed between AM and CM states (Fig. 13). The γ' phase exhibited a spherical morphology and uniform dispersion within the γ matrix. The mean particle sizes reached up to 55 nm and the volume fraction was

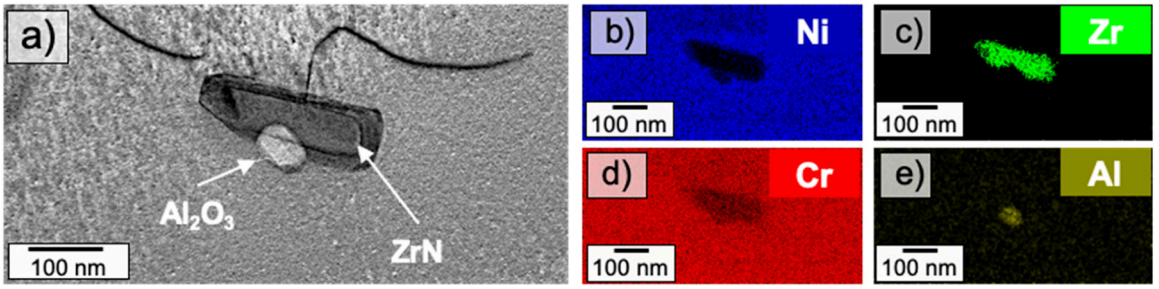

Fig. 6. TEM analysis of (a) ZrN and Al_2O_3 observed in AM state with a dislocation attached to the ZrN particle. The composition mapping of the precipitates and matrix shows the distribution of (b) Ni, (c) Zr, (d) Cr and (e) Al.

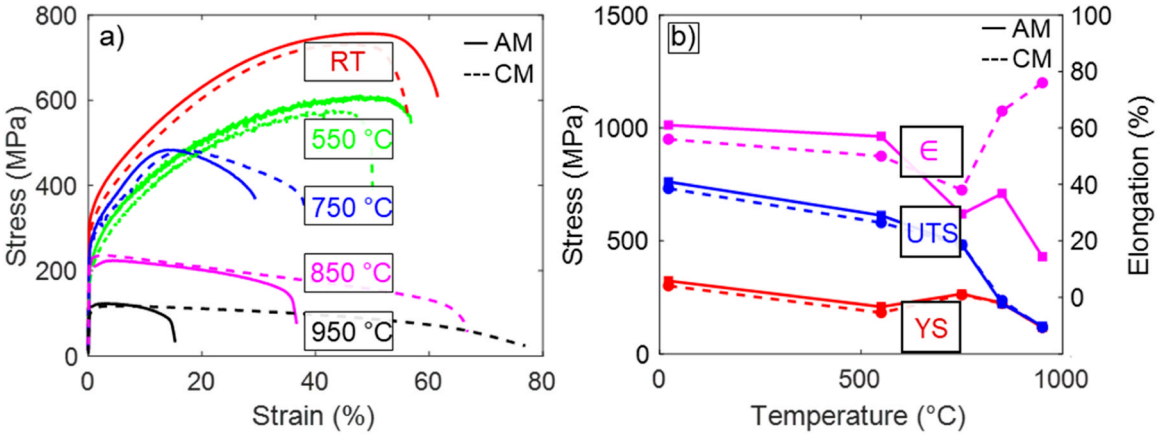

Fig. 7. Tensile properties of the AM and CM states at various testing temperatures. (a) Engineering stress- engineering strain curves. (b) Summary of the influence of testing temperature on ultimate tensile strength, yield strength, and elongation.

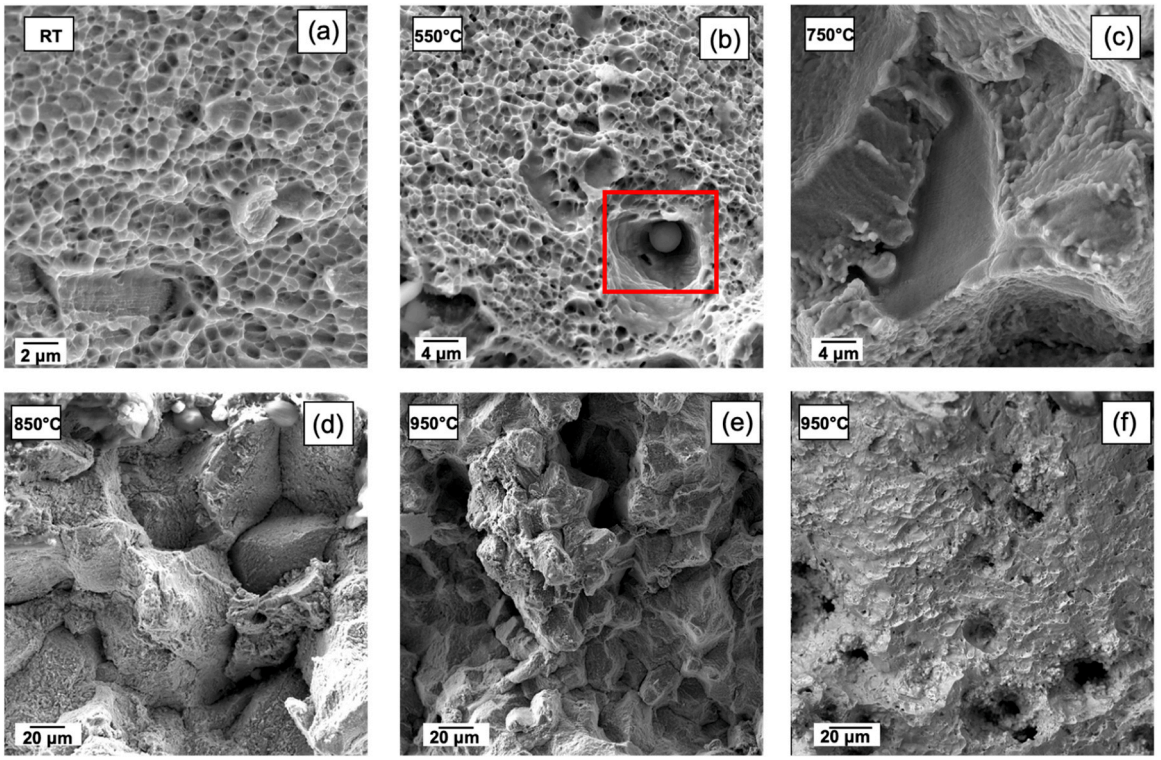

Fig. 8. Fractography analysis of AM state at (a) room temperature, (b) 550 °C, (c) 750 °C, (d) 850 °C, (e) 950 °C and (f) CM state at 950 °C, the inlet in (b) shows the unmelted powder particle.

measured to be 10.5 %, as detailed in Table 4.

The results of the SXRD measurements conducted on the AM state to analyse the precipitation kinetics are displayed in Fig. 14**a**. The analysis revealed that as the aging time was increased, additional phases started to emerge. To ascertain the corresponding phase for each peak, a comparison was made between the SHT condition and different aging conditions, as illustrated in Fig. 14**a**. It was found that with increasing annealing time, the peaks corresponding to γ' precipitates became more pronounced, as evidenced by the (110) superlattice reflection at 3.4°. The evolution of the volume fraction of γ' and $M_{23}C_6$ as a function of time is presented in the graph in Fig. 14**c**. These results were compared with the STEM analysis for γ' and SEM analysis for carbides, as presented in Table 4.

Additionally, the SEM and TEM analysis of AM state at 950°C and 25 MPa are depicted in Fig. 15. Notably, no γ' phase was detected. Instead, primary nanosized intragranular carbides were uniformly dispersed within the matrix, as illustrated in Fig. 15**b**. Furthermore, discrete intergranular $M_{23}C_6$ carbides were also observed, as shown in Fig. 15**a**. These findings were corroborated by elemental mappings, which revealed the persistent presence of Cr-rich carbides and oxide inclusions stemming from the AM process.

Towards a deeper understanding of the mechanisms governing creep behavior, a quantitative analysis utilizing inverse pole figure (IPF) mappings of the SHT and creep failed samples at 750 °C was performed, as shown in Fig. 16. The grain aspect ratio (GAR) and shape factor (F) were measured for the AM and CM states to understand the rate-controlling mechanism at 100 MPa. Notably, the differences between the shape factors remained minimal and the GAR confirmed the absence of elongated grains upon creep.

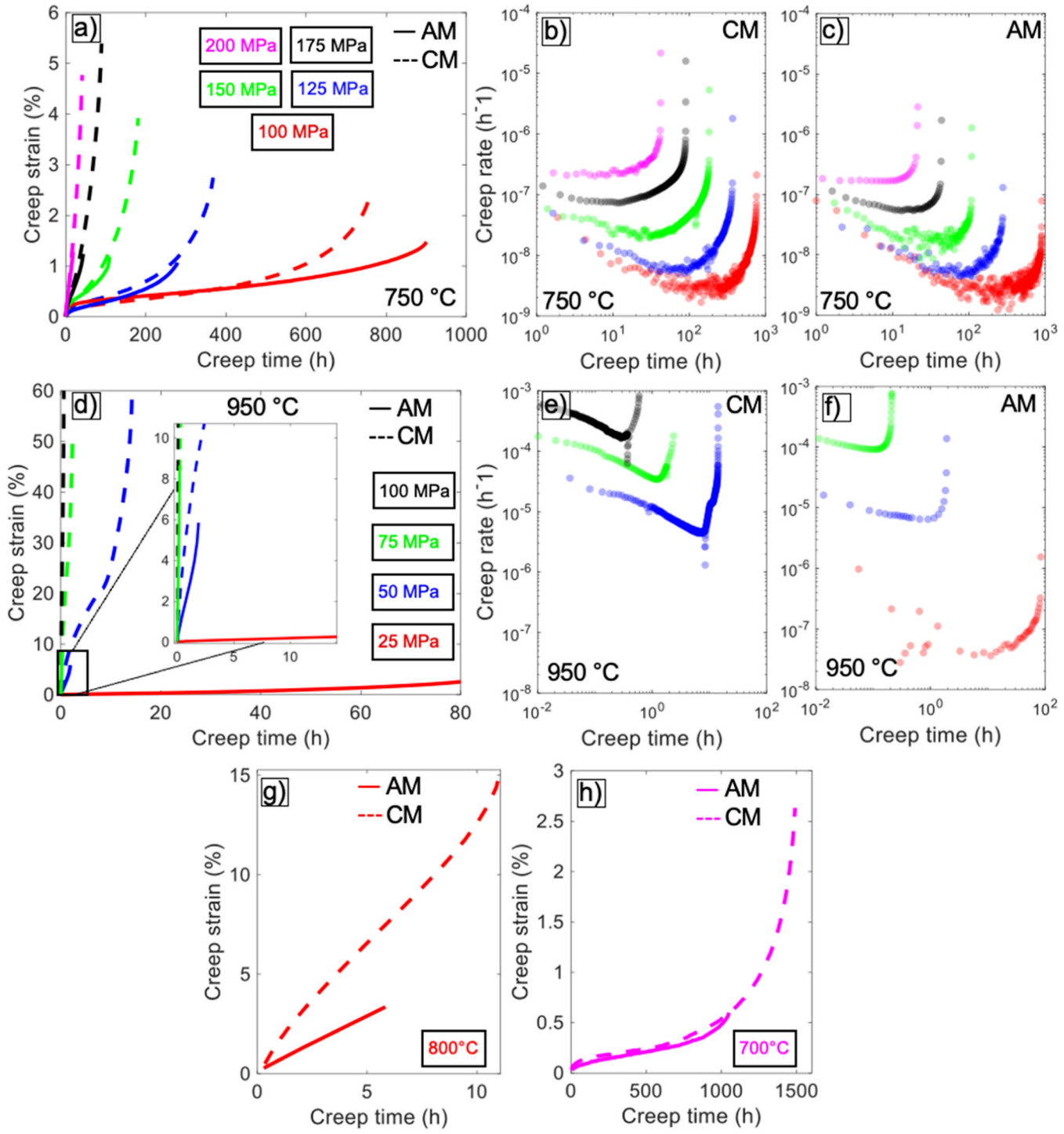

Fig. 9. Experimental results of the creep testing at 750 °C and 950 °C for AM and CM states. Creep strain (ϵ) - time (t) plots of CM and AM state at (a) 750 °C and (d) 950 °C under different applied stresses. Creep minimum strain rate ($\dot{\epsilon}$) – time plots (t) of (b) CM and (c) AM state at 750 °C and (e, f) 950 °C, respectively. Evolution of creep strain at 150 MPa for AM and CM states at (g) 800 °C and (h) 700 °C.

4. Discussion

The intricate laser material processing results in specific features associated with the AM process that exhibit heterogeneity. In this investigation, finer carbides, partial recrystallization, higher dislocation density, and smaller grain size were identified as distinctive heterogeneities specific to the AM state in this study.

4.1. Formation of heterogeneities during AM and SHT

During SHT, recrystallization resulted in the formation of fine equiaxed structures in AM and CM states (c.f Figs. 3 and 4). A majority of the grains in the microstructure exhibited annealing twins with Σ3 and Σ9 grain-boundaries attributed to the material's low stacking fault energy [72]. The high initial dislocation density in LPBF condition promoted static recrystallization during SHT. However, the incomplete recrystallization, fine grain sizes, and high dislocation density observed

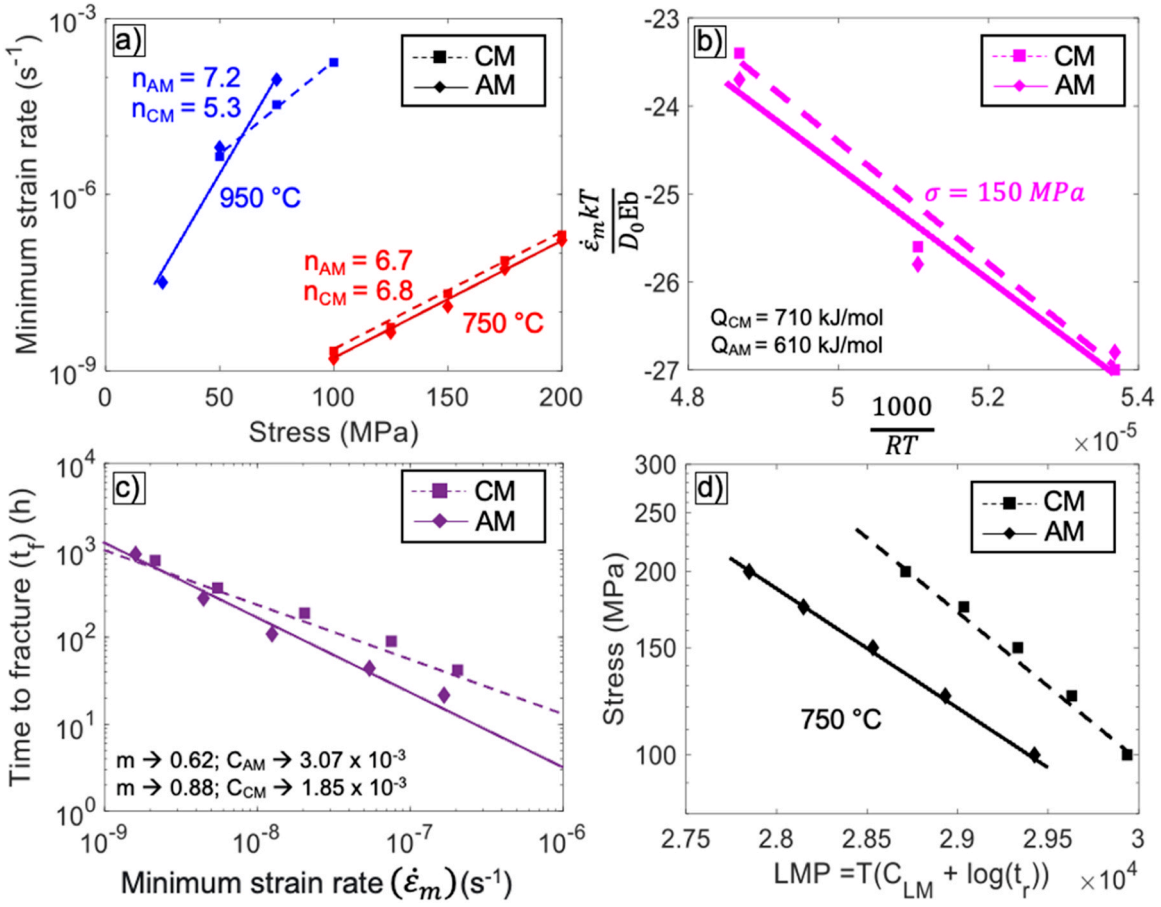

Fig. 10. Creep properties calculated based on the results of the creep experiments at 750 °C and 950 °C for AM and CM states. (a) Minimum strain rate - stress curves showing the stress exponent, (b) activation energy calculated based on Norton's creep law, (c) Monkmann-Grant relationship plot at 750 °C and (d) Larson-Miller parameter plot at 750 °C.

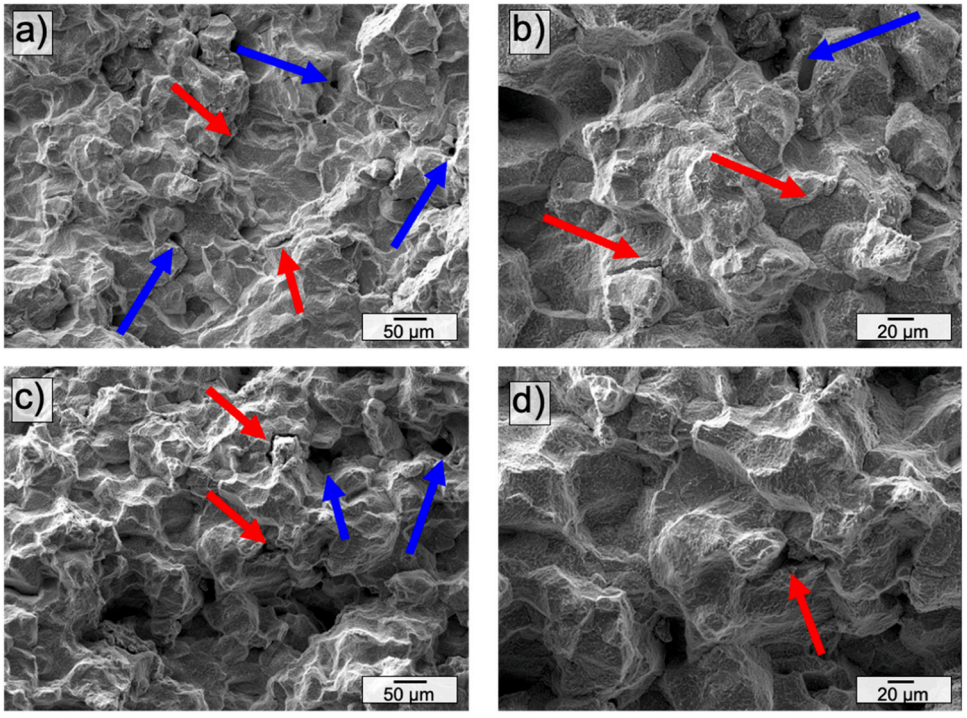

Fig. 11. Representative fracture surfaces of the creep-tested AM state at temperature and stress of (a, b) 750 °C and 125 MPa and (c, d) 950 °C and 50 MPa. The blue and red arrows indicate cavities and wedge cracks, respectively.

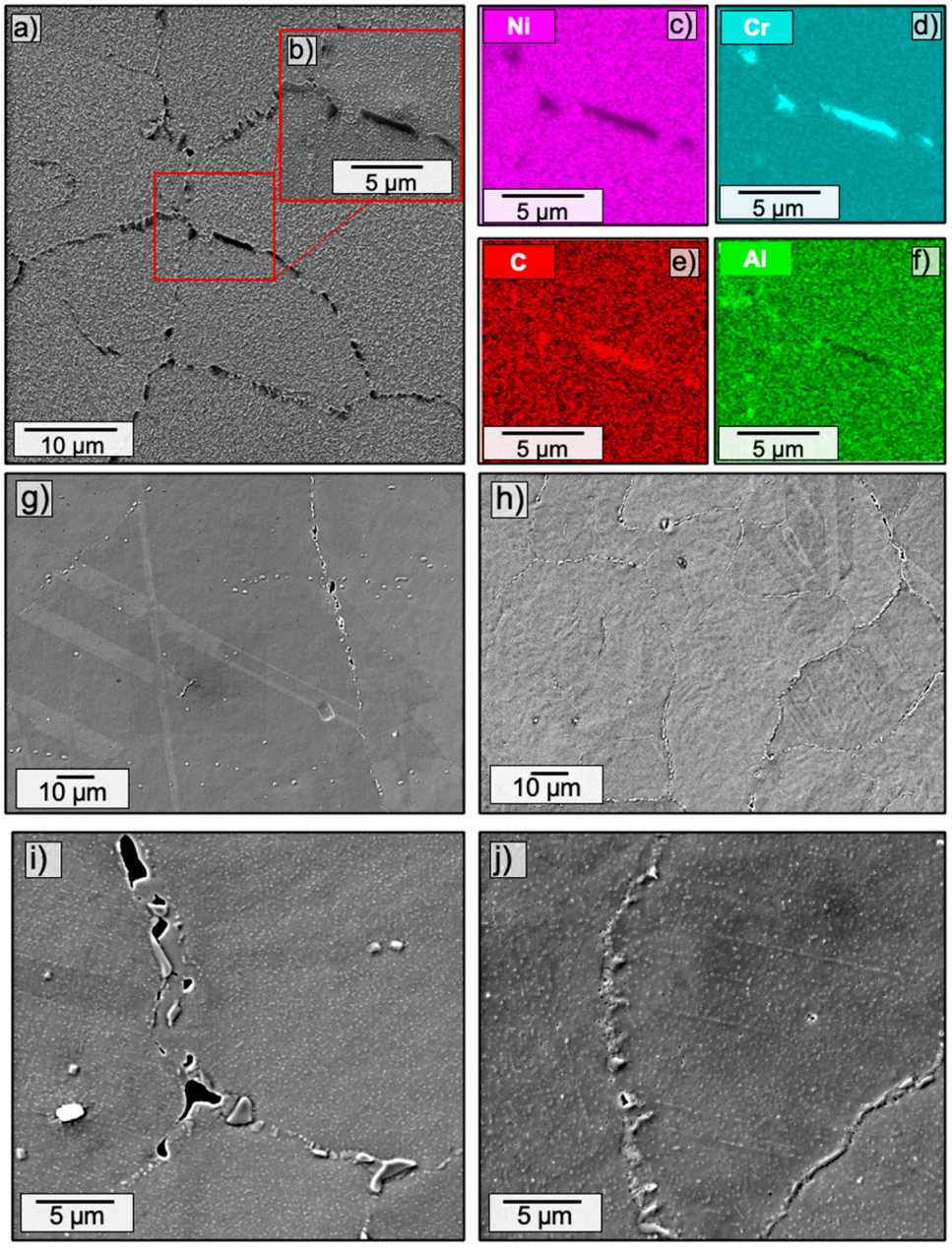

Fig. 12. (a) SEM and EDX analysis of AM state and exposure to a creep test (100 MPa) at 750 °C for 901 h, showing the decoration of grain-boundaries with $M_{23}C_6$ carbides. (b) The inset used for the EDX measurements, indicating the distribution of (c) Ni, (d) Cr, (e) C and (f) Al. SEM analysis of the distribution of grain-boundary ($M_{23}C_6$) carbides in (g, i) CM and (h, j) AM state after exposure to a creep test at 100 MPa and 750 °C.

in AM state were attributed to the difference in primary nanosized intragranular $M_{23}C_6$ carbide characteristics [73]. Notably, the CM alloy exhibited a higher volume fraction, lower number density, and coarser carbides compared to AM (c.f Fig. 5). These $M_{23}C_6$ carbides (mainly $Cr_{23}C_6$) are formed in a super-saturated solid solution as a result of high-temperature precipitation [74]. They are incoherent to the γ matrix and form through a eutectic-type reaction at the end of the solidification ($L + \gamma \rightarrow L + \gamma + M_{23}C_6$). The influence of these intragranular carbides on high-temperature mechanical properties, especially creep, becomes less significant as they dissolve and subsequently re-precipitate at the grain-boundaries during the progression of creep [75,76]. The disparity in carbide characteristics between CM and AM alloys was attributed to the high cooling rate and rapid solidification of the melt pool in AM state, which limited the precipitation and growth window of carbides during AM, resulting in a fine, dispersed distribution with a lower fraction [77]. These observations align with the findings of Liu et al. [78] and Davies et al. [37], where fine carbides were reported at high cooling rates. Additionally, it is important to note that during SHT of both AM and CM states, the carbides were not dissolved due to their high thermal stability. Consequently, pinning of grain-boundaries by carbides (c.f Fig. 5**b,e**) prevented complete recrystallization as well as grain growth in AM state [26]. However, in CM state, the pinning force was reduced due to the lower number density and larger carbide sizes. In addition due to the high pre-deformation, the CM state exhibited complete recrystallization leading to lower dislocation density as well as larger grains and a lower fraction of annealing twins after SHT [79]. A complete recrystallized structure in AM state can be achieved by facilitating the growth of carbides through a modified heat treatment. Messe et al. [80] combined stress relief heat treatment with a SHT in IN738LC to enable the growth of fine primary intragranular carbides from 50 to

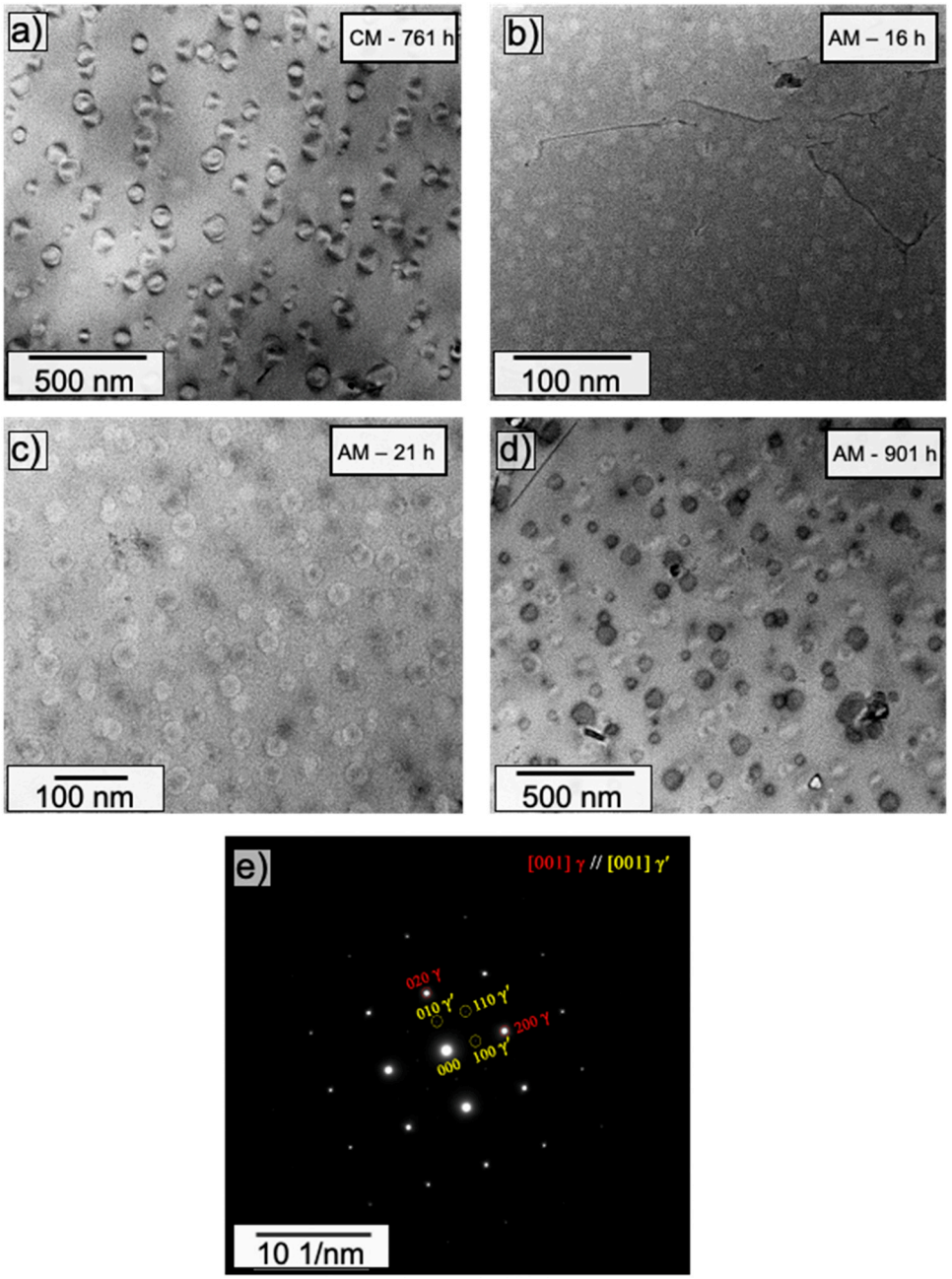

Fig. 13. STEM analysis of the evolution of γ' in CM and AM state aged at 750 °C for different time periods. (a) CM state after creep exposure for 761 h (100 MPa), AM state after aging for (b) 16 h, (c) 21 h, (d) creep exposure for 901 h (100 MPa) and (e) SAED pattern measured at the precipitate showing superlattice reflection of γ' in γ matrix.

200 nm in the as-built state to 1.5 μm, and thus, achieved complete recrystallization.

4.2. Correlation between heterogeneities and mechanical properties

4.2.1. Tensile properties

During tensile testing, the normal and inverse dynamic strain aging (DSA) or Portevin-Le Chatelier effect (PLC) was observed, especially at 550 °C and 750 °C, in both AM and CM states, probably due to the presence of C-Cr complexes, and Cr atoms. This effect has been reported in several studies on CM high-Cr Ni-based alloy [81–83]. It was seen that the yield strength of the alloy decreased with temperatures except at 750 °C, while the ultimate tensile strength (UTS) of both AM and CM states exhibited a consistent drop with increasing temperature. The temperature anomaly was caused by the onset of γ' precipitation. Even a short period of stabilization at temperature before the beginning of the test was sufficient to produce a small volume fraction of γ' precipitates (Fig. 14**c**). Furthermore, the drop in ductility of CM and AM state at 750°C was explained by the ductile-brittle mixed failure mode (c.f Fig. 8**c**).

At temperatures exceeding 750°C, both AM and CM alloy displayed a reduction in yield strength, as they surpassed the solvus temperature of the γ' phase, leading to the absence of precipitation strengthening. Furthermore, the CM state consistently displayed higher ductility than the AM state and the elongation of both the alloys increased with temperature due to the dissolution of γ' phase. The low elongation characteristic of AM state at 850°C and 950°C was explained by intergranular fracture observed at 850°C and 950°C (Fig. 8**d** and Fig. 8**e**). This

Table 4
Size and volume fraction of carbides and γ' phase at 750 °C in AM and CM states determined by STEM and SXRD analysis.

Aged	0.5 h	1 h	16 h			21 h	
	SXRD - γ' vol (%)	SXRD - γ' vol (%)	SXRD - γ' vol (%)	STEM - γ' vol (%)	size (nm)	STEM - γ' vol (%)	size (nm)
AM	0.10	2.30	6.60	7.50	7.05	8.40	21.39

Aged	AM - 901 h / CM – 761 h					
	SXRD - γ' vol (%)	STEM - γ' vol (%)	size (nm)	SXRD - $M_{23}C_6$ carbides vol (%)	SEM - $M_{23}C_6$ carbides (GB) vol (%)	size (nm)
AM	10.90	12	51.30	2.20	2.32	625.00
CM	-	10.80	53.50	-	1.52	1257.00

embrittlement behavior of Ni-based alloys at elevated temperatures has been extensively documented in the literature, with factors including monotonic oxygen-induced embrittlement, sulfur-induced intergranular fracture, and secondary phase precipitation at grain-boundaries contributing to this phenomenon [33]. Nevertheless, in this investigation, the residual oxygen stemming from the AM process and powder production as seen from the combustion analyzer resulted in the formation of oxides (c.f Fig. 6 and Fig. 15**c**) as well as enrichment in the grain-boundaries (c.f Fig. A.3), leading to embrittlement at high temperatures (Fig. 7). Risse et al. [84] similarly observed the enrichment of grain-boundaries with Al_2O_3 in AM IN738LC through atom probe tomography due to the presence of oxygen in the LPBF process or in gas atomization. In the current study, the oxides were not dissolved during the SHT due to their high melting point. In addition, prolonged exposure to high temperatures as seen in Fig. A.3, led to the depletion of Al at grain-boundaries, with Al migrating towards the matrix, subsequently forming γ'.

4.2.2. *Creep properties*

Creep behavior of AM and CM states demonstrated high n values (6.7–6.8 at 750 °C and 5.3–7.2 at 950 °C) as seen in Fig. 10**a**, indicating a dislocation-climb-controlled creep mechanism [85]. It is worth noting that the activation energy for the polycrystalline Ni alloys is typically 300 kJ/mol [86]. However, the observed activation energies were much higher, as seen in Fig. 10**b**. The observed high activation energy and stress exponents were attributed to the resistance of dislocation glide from γ' precipitates in the matrix, which precipitated during creep (in situ) at 750 °C (c.f Fig. 13 and Fig. 14). Furthermore, grain-boundary carbides acted as "dispersive" obstacles, retarding grain-boundary sliding and forming barriers to crack propagation, resulting in the extension of the high-temperature rupture life and an improvement in creep rate (c.f Fig. 12). The difference in the activation energy between the AM and CM states at 150 MPa, as seen in Fig. 10**b** was due to the differences in the microstructures of AM and CM alloys, especially the grain-boundary density [37]. The increased grain-boundary density, as observed in AM state (c.f Fig. 4**e**), led to reduced activation energy.

4.2.2.1. *Effect of grain size on the creep behavior at 750 °C.*

In AM state,

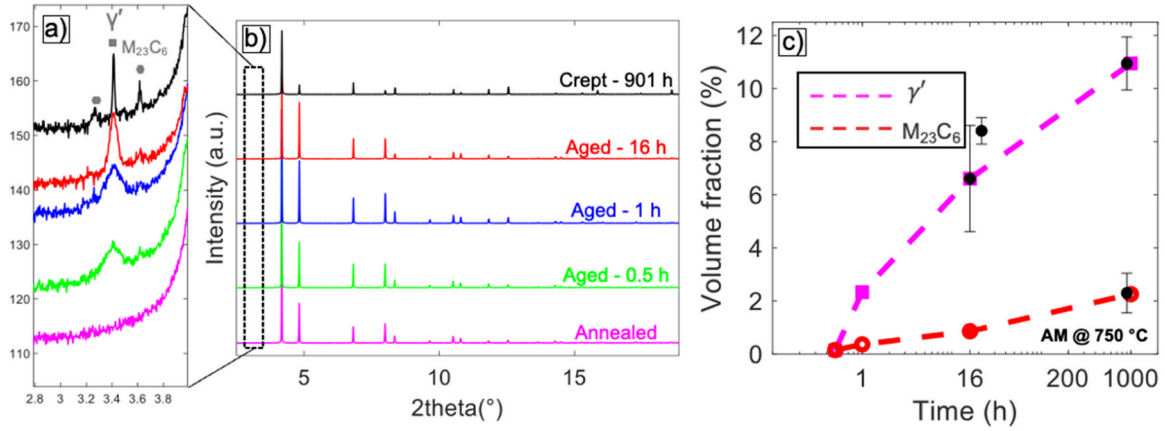

Fig. 14. SXRD analysis of the evolution of γ' and carbides ($M_{23}C_6$) in AM state aged at 750 °C for 0.5 h, 1 h, 16 h and 901 h. (a) The inset shows the superlattice reflection of γ' as well as the $M_{23}C_6$ carbides. (c) The evolution of the volume fractions of γ' and carbides determined by SXRD (dashed lines) and the corresponding values measured by STEM (black dots), as previously presented in Fig. 13.

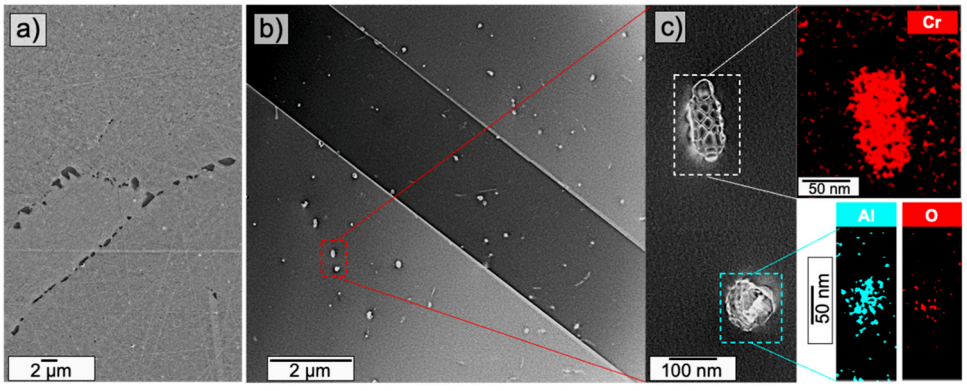

Fig. 15. Microstructure characterization of AM state after creep failure at 25 MPa and 950 °C. (a) SEM analysis showing the discrete distribution of grain-boundary $M_{23}C_6$ carbides and (b, c) TEM analysis of the intra-granular carbides and oxides.

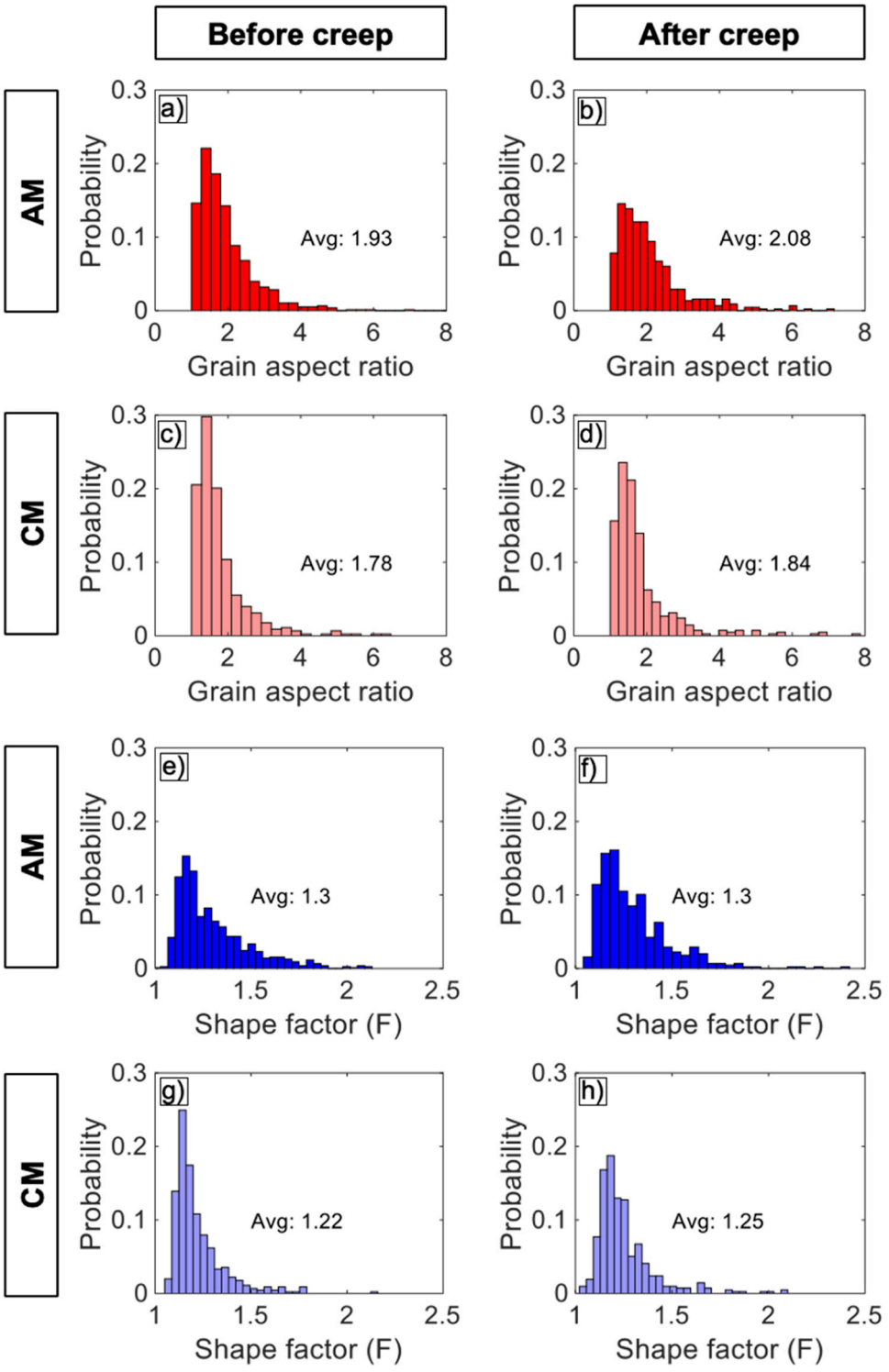

Fig. 16. Grain-structure analysis based on EBSD data of the AM and CM states obtained before creep testing and after creep failure at 750 °C and 100 MPa stress.

the grain-boundaries served as significant dislocation obstacles during the secondary creep regime, leading to a significant reduction in creep rates under the prevailing mechanical conditions. Since both the alloys exhibited similar fractions of γ', the difference in the minimum strain rate was accounted for the difference in grain sizes. Thebaud et al. [87] found that at 700 °C, the creep strain rate of a single-crystalline Ni-based superalloy was inferior compared to coarse- and fine-grained structures, which was attributed to the strengthening effect of grain boundaries, especially at strains less than 1 %. Furthermore, the AM state exhibited an inferior creep life and ductility compared to the CM state at both 750 °C (except at 100 MPa) and 950 °C. During creep, no significant changes in grain size were observed due to the presence of $M_{23}C_6$ carbides distributed along the grain boundaries (c.f Fig. 12 and Fig. 15), effectively hindering grain-boundary migration at 750 °C and 950 °C for both AM and CM states. This confirms the absence of dynamic recrystallization in the partially recrystallized areas of the AM state during creep. It was primarily because of the low strain level formed during creep (as low as 1.5 %) and the moderate temperatures, leading to the exclusion

of dynamic recrystallization as a rate-controlling mechanism in this study. Furthermore, Σ3 grain-boundaries can serve to retard or divert crack propagation due to the significant reduction in the random grain-boundary network length (RGBN) [37]. However, both AM and CM states displayed a similar fraction of twin boundaries (56 % and 58 % respectively), indicating RGBN cannot explain the difference in the creep behavior.

During creep deformation controlled by dislocation climb and glide, the deformation leads to cavity formation, eventually resulting in creep rupture. The growth and interlinkage of these cavities lead to creep failure. During creep, cavities nucleate due to vacancy accumulation, dislocation pile-up against the stress-concentrated regions, such as grain boundaries or hard particles or due to grain-boundary sliding [70]. The cavity-nucleation rate depends on the potential nucleation sites and the stress acting across the grain boundaries transverse to the loading direction. At 750 °C, the intracrystalline strength of the material increased with the duration of the creep test due to a gradual increase of volume fraction of γ' precipitates in the matrix (c.f Fig. 13 and Fig. 14). Meanwhile, the diffusion of point defects (vacancies) and the subsequent formation of cavities predominantly weakened the grain boundaries, leading to strain incompatibility at these boundaries and resulted in intercrystalline fracture. This was supported by the representative fracture surfaces of specimens subjected to creep tests at 750 °C and 950 °C exhibiting wedge cracks and cavities, as shown in Fig. 11. Moreover, fine grains have a greater number of cavity nucleation sites per unit volume compared to coarse grains (c.f Fig. 17**a** and **b**). This accelerated cavity formation, interlinkage of cavities led to a faster rate of crack propagation and, ultimately, premature failure in AM state. Thus, the lower creep resistance exhibited by AM state was strongly attributed to the disparity in grain size at both 750 °C and 950 °C. Furthermore, fine grains offer a greater grain-boundary area per unit volume, enlarging potential crack initiation sites. In addition, grain-boundaries tend to be flatter in the fine-grain region than in the coarse-grain areas, which makes crack propagation easier [25,70]. The time to fracture for AM state at stresses ≥ 175 MPa was nearly 50 % shorter than in CM state, whereas at lower stresses, the difference was only about 25 %. Since the nucleation and growth rate of cavities are highly influenced by the applied stresses at high temperatures, the accelerated nucleation and growth of cavities resulted in early failure for AM state. The microstructural heterogeneity resulting from the AM process significantly influenced the creep behavior through variation in grain size. While increasing grain size might typically enhance creep resistance, this proposition encounters challenges with AM-produced alloys due to the presence of fine carbides. Zhao et al. [88] conducted a study focusing on the effect of homogenization treatment at 1180 °C for Alloy 718, with treatment durations ranging from 1 to 12 h. Intriguingly, the findings revealed that the fine carbides generated during AM remained unaffected by the treatment and exhibited virtually no change in grain size over the studied duration. In stark contrast, CM alloys exhibited a significant increase in grain size under similar conditions [88]. This distinction underscores the unique microstructural characteristics of AM-produced alloys, which present challenges in optimizing their creep behavior.

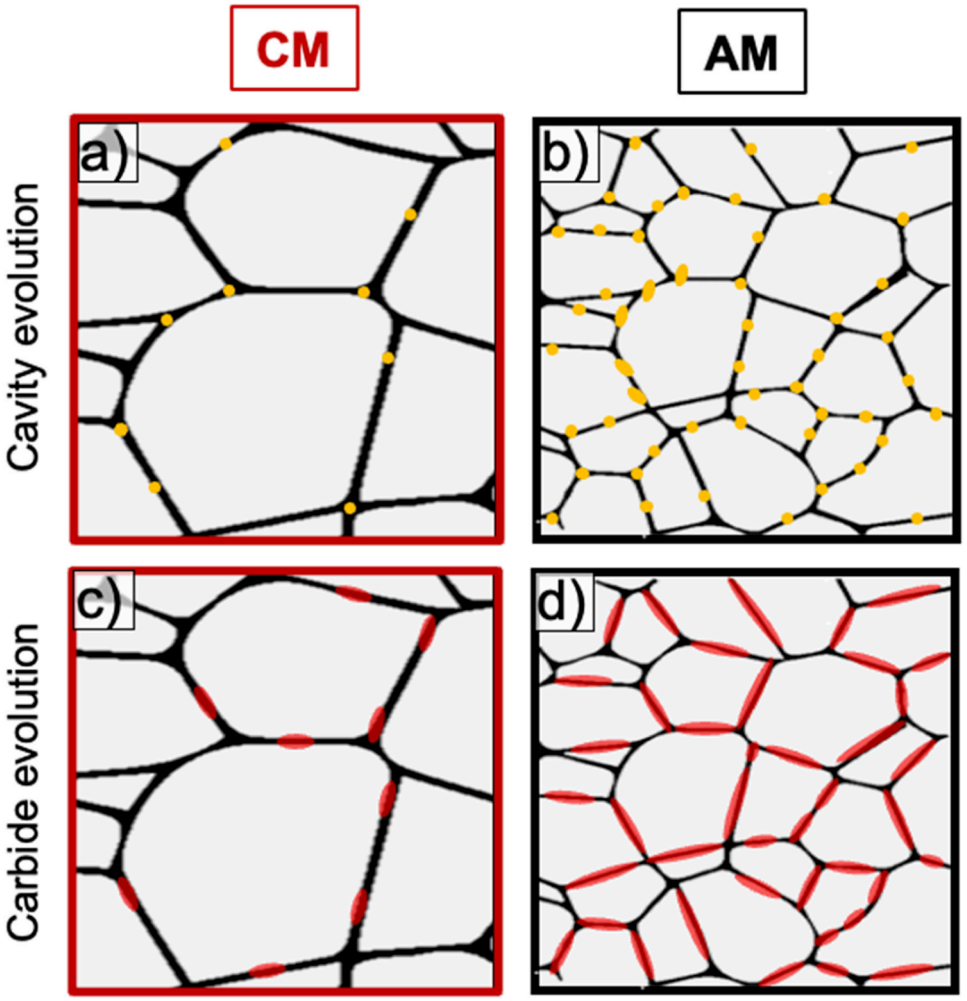

Fig. 17. Evolution of (a, b) creep cavities (yellow markers) and (c, d) grain boundary $M_{23}C_6$ carbides (red markers) for CM and AM state.

4.2.2.2. Effect of carbide distribution on the creep behavior at 750 °C. While the creep behavior remained consistent up to 125 MPa, at low stress levels (100 MPa), the AM alloy exhibited better or comparable performance than the CM state at 750 °C. To confirm this behavior and to account for the common 5 % scattering of results observed in general during creep tests, additional tests at 100 MPa were conducted, and it was confirmed that the time-to-rupture was still improved for the AM state (13 %-19 %) compared to the CM state. This suggested that, in addition to creep cavitation, a different mechanism contributed to the improved creep behavior of AM state. Notably, the findings revealed a conspicuous absence of grain elongation in both AM and CM specimens following creep at 100 MPa and 750 °C. Instead, the grain structure revealed an equiaxed configuration, as inferred by GAR in Figs. 16**b and** 16**d**. The shape factor F (c.f Fig. 16**f and h**) and GAR consistently indicated a close resemblance to equiaxed grain structures in both pre-creep and post-creep states for both AM and CM states. The lack of substantial grain growth or alterations in GAR (c.f Fig. 16) at these test temperatures and stresses confirmed that extensive boundary migration was absent [89]. This congruity strongly suggested that grain-boundary sliding played a significant role in the overall deformation process during creep. The minor differences observed in GAR and F were primarily attributed to the initial minor grain growth, which persisted until a critical density of intergranular carbides precipitated, subsequently impeding further grain-boundary migration [90].

Moreover, the presence of intergranular $M_{23}C_6$ carbides, as observed in both AM and CM states, effectively inhibited the movement of grain boundaries, furthermore, strengthening resistance to grain-boundary sliding. During creep testing at 750 °C, the primary nanosized intragranular carbides underwent dissolution and subsequent re-precipitation as $M_{23}C_6$ carbides at the grain boundaries. The application of tensile stress, in conjunction with the optimal temperature, accelerates the precipitation process by creating a significant driving force for the nucleation and growth of secondary carbides [91]. These $M_{23}C_6$ carbides impeded the grain-boundary sliding and grain growth during creep testing through a pinning effect, as seen in Fig. 12**a**. Upon comparing the SEM analysis of the $M_{23}C_6$ carbides formed at the grain boundaries for the post-creep specimens (c.f Fig. 12), a significant distinction became evident (c.f Fig. 17**c and d**). The AM alloy demonstrated the presence of finely distributed carbides consistently along the grain boundaries (c.f Fig. 17**c**). In contrast, the CM state revealed the formation of coarse, granular, and distinct carbides along the grain boundaries (c.f Fig. 17**d**). The disparity in grain size between AM and CM states leads to variations in the precipitation of carbides along the grain boundaries. In CM state, where larger grain sizes were present, there was relatively less surface area available for precipitate formation. Ideally, thicker and more continuous films of precipitates are expected in larger grains [92]. However, contrary to this expectation, the opposite phenomenon was observed, mainly due to entrapment of carbon in the undissolved coarse intragranular carbides. The formation of $M_{23}C_6$ carbides involves the diffusion of Cr and C to the grain boundaries, originating from two sources: (1) C and Cr dissolved in the matrix and (2) dissolution of intra-granular carbides. However, in CM state, the presence of primary coarse intra-granular carbides, as depicted in Fig. 5**a** and 5**b**, prevented their complete dissolution even after 761 h, leading to the absence of a uniform network of carbides. The long-term exposure of CM state at 700 °C for 5000 h confirms furthermore that the intra-granular carbides remain un-dissolved in the CM state [93]. In contrast, in the AM state, no intra-granular carbides were observed in the STEM and SEM analysis (c.f Fig. 12, Fig. 13**b-d**), indicating their complete dissolution and transformation into grain-boundary carbides. Furthermore, in the AM state, there was a slight persistence of C and Cr segregation even after SHT (c.f Fig. 2**c, d**), which furthermore promoted the precipitation kinetics of $M_{23}C_6$ carbides. Additionally, the finer grain sizes observed in AM state led to an increased density of nucleation sites for $M_{23}C_6$ [94], resulted in the formation of finer grain-boundary carbides. In addition to grain size disparity, the difference in intra- and inter-granular carbide distribution between the AM and CM states was characterized as a heterogeneity induced by the AM process. These carbides serve as potential hindrances to grain-boundary mobility, thereby enhancing resistance to grain-boundary sliding [37]. The differences in carbide dimensions led to noticeable contrasts in the extent of grain-boundary sliding between the two states. It is imperative to recognize that grain-boundary sliding can manifest in two ways: (a) through dislocation motion involving glide and climb within the matrix or (b) via grain-boundary diffusion. The inability to effectively facilitate grain-boundary sliding inevitably leads to the creation of cavities or creep fissures, ultimately culminating in creep failure. As a consequence of the marked disparity in carbide distribution, the AM state exhibited a considerably extended creep life. This observation indicated that the intergranular carbides governed the transient creep behavior at long exposure times. However, it is worth noting that the impact of grain-boundary carbides on extending creep lifetime significantly diminished at higher stress levels, where cavitation emerged as the primary rate-controlling mechanism. Although certain studies had reported the migration of grain-boundary carbides in regions subjected to compressive stresses [75,90], this study did not observe such migration. Instead, a uniform distribution of carbides was evident in both AM and CM states after creep. El-Magd et al. [95] confirmed that though carbide precipitation occurred more rapidly under higher stresses, the carbides governed creep behavior primarily at lower stress levels. Furthermore, the larger sizes of the carbides found in the grain-boundary accelerated the inter-granular cracking behavior for the CM state compared to the AM state [96].

Hence, a complex interplay of diverse strengthening mechanisms, including grain-boundaries, intragranular γ' precipitates, intragranular and intergranular $M_{23}C_6$ carbides, as well as the influence of oxides, contributes to the overall mechanical behavior of NiCrAl alloy. The specific mechanism in operation varies depending on factors such as applied temperature and stress conditions, also as confirmed by the simulations [64].

4.2.2.3. Rate-controlling mechanism at 950 °C. At 950 °C, there was no γ' precipitation in the alloy since its solvus temperature is slightly above 800 °C (c.f Fig. 15**b**). The absence of γ' precipitates in the matrix eliminates the intracrystalline reinforcement. Therefore, the intragranular and intergranular carbides ($M_{23}C_6$) govern the creep properties at 950 °C and in addition also the grain size (c.f Fig. 15) [81]. It is worth noting that at 50 MPa, the CM state had a lifetime of 14.18 h, while the AM state had a lifetime of merely 2 h. The smaller grain size, low fraction of intra granular carbides and presence of oxides in AM state promoted enhanced grain-boundary sliding and exhibited a poor resistance to crack propagation. These microstructural features controlled the creep behavior at 950 °C as confirmed by much lower creep life at 950 °C (80 % lower at 50 MPa) compared to at 750 °C (45 % lower) for the AM state with respect to the CM state. Furthermore, the resistance of grain boundaries to deformation was weakened as the coalescence of vacancies at structural inhomogeneities like oxides or carbides at grain boundaries was accelerated. The presence of wedge cracks on the fracture surfaces confirms that the rupture was intercrystalline (c.f Fig. 11).

5. Conclusions

The study conducted provides a comprehensive investigation of the creep and tensile behavior of the γ'-forming Ni-based Alloy 699XA, produced by both additive manufacturing (AM) and conventional manufacturing (CM) processes. The investigation of the creep behavior covered a range of temperatures from 750°C to 950°C and stress levels from 25 MPa to 200 MPa up to 1500 h. The study integrated various characterization techniques, including SEM, EBSD, SXRD, and TEM, to elucidate the microstructural evolution and to reveal the underlying high-temperature creep mechanisms. From this in-depth analysis, the

following key conclusions can be drawn:

1. The complex interplay of laser-material interactions, non-equilibrium solidification processes, and rapid cooling rates led to distinct microstructural attributes in AM, which were retained even after a solution heat treatment (SHT). Notably, AM led to the formation of fine intragranular primary $M_{23}C_6$, ZrN, and Al_2O_3 precipitates as compared to CM, where only coarse carbides were formed. The fine $M_{23}C_6$ carbides impeded grain-boundary movement during subsequent solution heat treatment (SHT) and caused a partially recrystallized microstructure and finer grain size.
2. The complete dissolution of fine primary carbides in AM state upon creep at 750 °C led to fine uniform continuous inter-granular carbides, unlike coarse, discontinuous distributed carbides along the grain-boundary in CM. In contrast, γ' formation and Cr distribution were similar in AM and CM due to the SHT.
3. The presence of AM-specific fine aluminum oxides led to a lower elongation-to-fracture with increasing temperature (or at high temperature) of the AM state. Despite inhomogeneity in the precipitation of secondary grain-boundary $M_{23}C_6$ during creep at 750 °C, the similar precipitation kinetics of γ' between AM and CM conditions controlled the primary and secondary creep regimes leading to similar minimum and steady-state creep strain rates. In contrast, primary intragranular carbides controlled the creep at 950 °C due to the absence of γ' formation. However, smaller grain sizes led to accelerated tertiary creep at high stress and poor creep life of the AM state.

CRediT authorship contribution statement

Christian Haase: Writing – review & editing, Supervision, Methodology. **Johannes Henrich Schleifenbaum:** Writing – review & editing, Supervision. **Ulrich Krupp:** Writing – review & editing, Supervision, Funding acquisition. **Frederike Brasche:** Writing – review & editing, Supervision, Conceptualization. **Ivo Šulák:** Writing – review & editing, Methodology, Investigation, Conceptualization. **Venkatesh Pandian Narayana Samy:** Writing – review & editing, Writing – original draft, Visualization, Software, Methodology, Formal analysis, Data curation, Conceptualization. **Zdeněk Chlup:** Methodology, Investigation. **Tomáš Záležák:** Methodology, Investigation, Formal analysis. **Bhupesh Verma:** Writing – review & editing, Resources. **Benedikt Nowak:** Writing – review & editing, Resources, Investigation.

Declaration of Competing Interest

The authors declare that they have no known competing financial interests or personal relationships that could have appeared to influence the work reported in this paper.

Data Availability

Data will be made available on request.

Acknowledgements

The authors would like to thank Betül Bezci, RWTH Aachen University, Steel institute, Germany for valuable discussions and analysis on the experiments. The authors would like to acknowledge DESY (Hamburg, Germany), a member of the Helmholtz Association HGF, for the provision of experimental facilities. Synchrotron XRD experiments in the research were carried out at Petra III and we would like to thank Dr. Efthymios Polatidis at Paul Scherrer Institut and Ahmet Turnali at RWTH Aachen University. Beamtime was allocated for proposal I-20220679 EC. This research is supported by the funding from the European Union's Horizon 2020 research and innovation program under grant agreement No 958192. CH also acknowledges the support of the German Federal Ministry of Education and Research within the NanoMatFutur project "MatAM - Design of additively manufactured high-performance alloys for automotive applications" (project ID 03XP0264).

Appendix

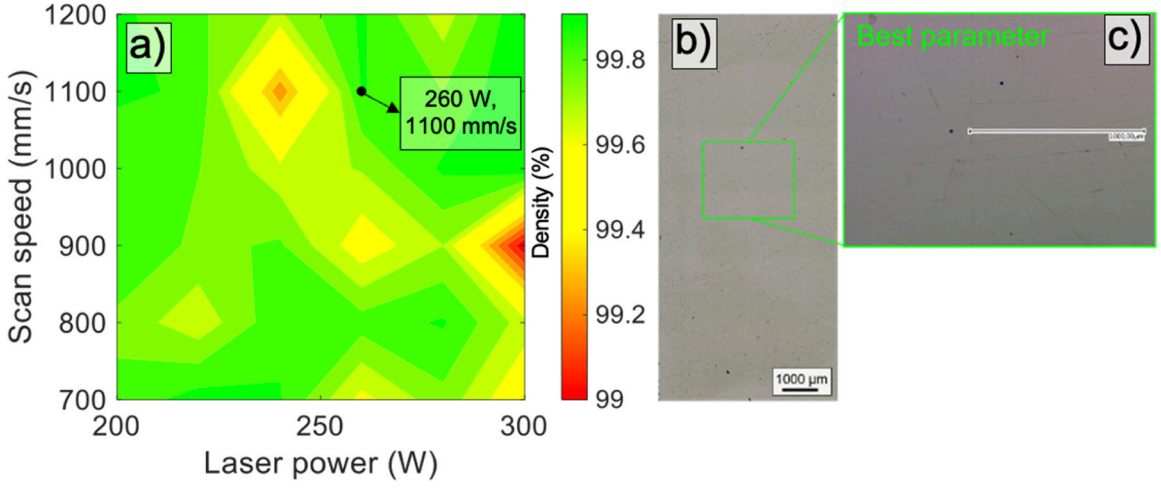

Fig. A.1. Process parameter development for AM state. (a) Effect of laser power and laser scan speed on relative density, as determined by optical microscopy. The best parameter resulted in a relative density of 99.57 %. (b) Optical micrographs of the best parameters, along with a zoomed-in section for a more detailed view.

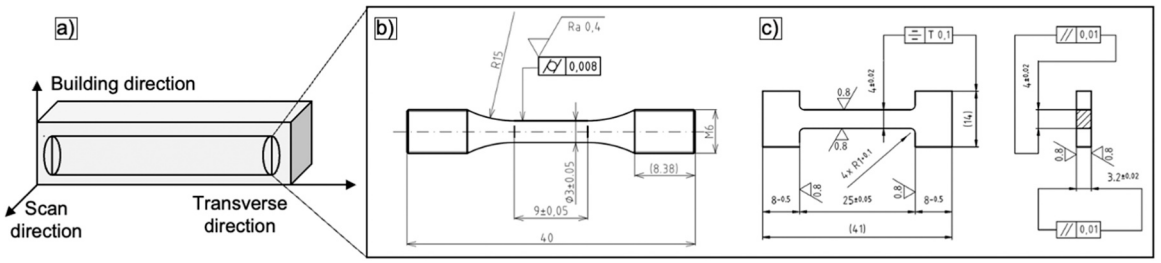

Fig. A.2. Geometry of samples used for mechanical testing. (a) The samples were extracted from a large cuboid along the transverse direction. Geometry of testing specimens used for (b) tensile experiments and (c) creep experiments.

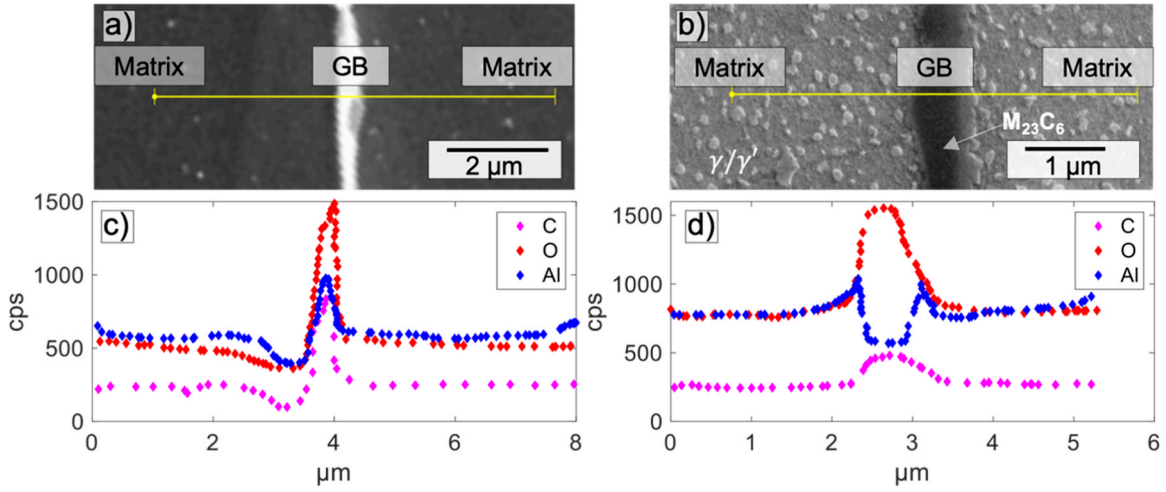

Fig. A.3. EDX analysis of the AM state. Line analysis showing the oxygen enrichment at the grain boundaries after (a) SHT and (b) additional creep testing at 750 °C for 901 h.

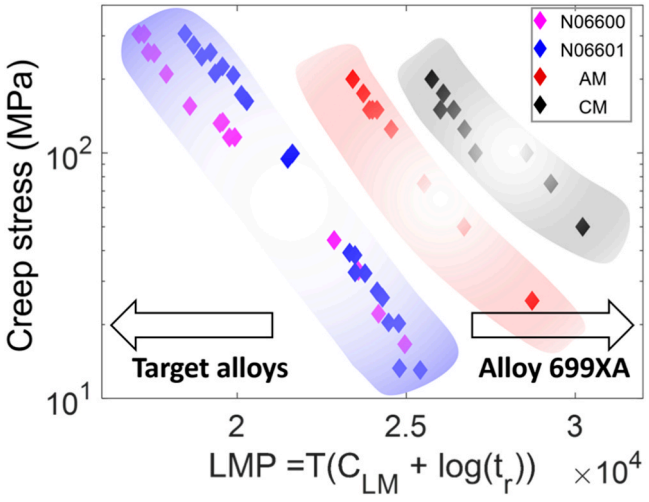

Fig. A.4. Larson-Miller parameter map of the AM and CM states compared with UNS N06600 and UNS N06601 [20].

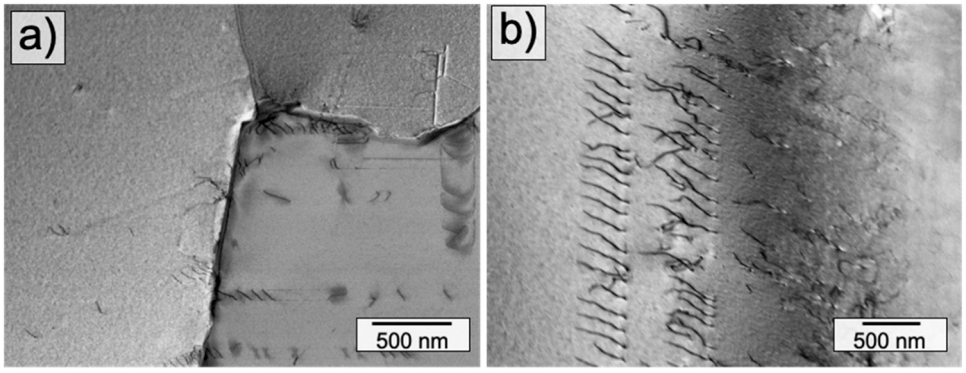

Fig. A.5. Dislocation density characterized for SHT CM and AM state.

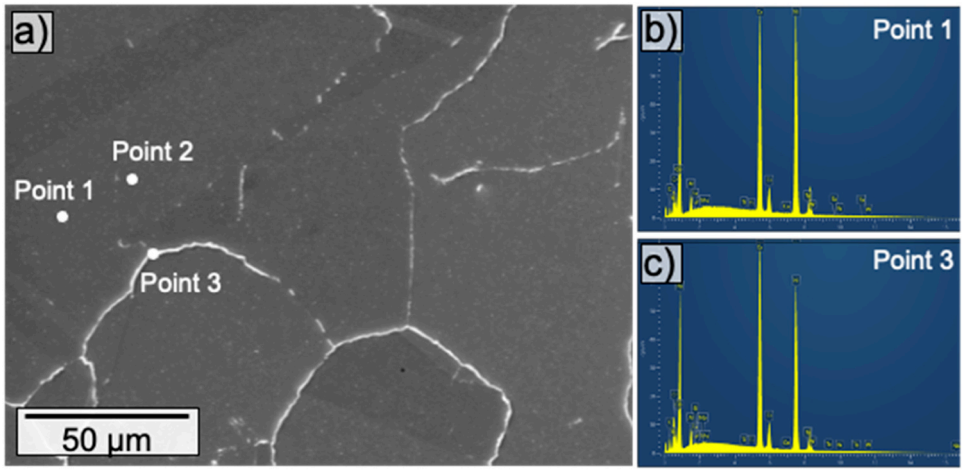

Fig. A.6. SEM-EDX point analysis of SHT AM state: (a) SEM image; EDX spectroscopy analysis of (b) Point 1 (matrix) and (c) Point 3 (grain boundary).

Table A.1
EDX point analysis of SHT AM state. Measurement points are indicated in Figure A.6.

Site	Point	Ni	Al	Cr	Nb
Matrix	Point 1	bal.	2.13	27.95	-
	Point 2	bal.	2.09	27.92	0.18
Grain boundary	Point 3	bal.	2.35	31.78	0.18

References

[1] C. Panwisawas, Y.T. Tang, R.C. Reed, Metal 3D printing as a disruptive technology for superalloys, Nat. Commun. 11 (2020) 2327, https://doi.org/10.1038/s41467-020-16188-7.
[2] D. Karlsson, C.-Y. Chou, N.H. Pettersson, T. Helander, P. Harlin, M. Sahlberg, G. Lindwall, J. Odqvist, U. Jansson, Additive manufacturing of the ferritic stainless steel SS441, Addit. Manuf. 36 (2020) 101580, https://doi.org/10.1016/j.addma.2020.101580.
[3] Z. Tian, C. Zhang, D. Wang, W. Liu, X. Fang, D. Wellmann, Y. Zhao, Y. Tian, A review on laser powder bed fusion of inconel 625 nickel-based alloy, Appl. Sci. 10 (2020), https://doi.org/10.3390/app10010081.
[4] E. Hosseini, V.A. Popovich, A review of mechanical properties of additively manufactured Inconel 718, Addit. Manuf. 30 (2019) 100877, https://doi.org/10.1016/j.addma.2019.100877.
[5] S. Sanchez, P. Smith, Z. Xu, G. Gaspard, C.J. Hyde, W.W. Wits, I.A. Ashcroft, H. Chen, A.T. Clare, Powder Bed Fusion of nickel-based superalloys: a review, Int. J. Mach. Tools Manuf. 165 (2021) 103729, https://doi.org/10.1016/j.ijmachtools.2021.103729.
[6] B. Cheng, C. Liu, M. Song, A comparison of the microstructures and mechanical properties of a GH648 superalloy fabricated by selective laser melting and casting, Mater. Sci. Eng.: A 813 (2021) 141178, https://doi.org/10.1016/j.msea.2021.141178.
[7] B. Cheng, J. Gu, M. Song, An investigation of the microstructural evolution and tensile properties of a nickel-based GH648 superalloy manufactured through selective laser melting, Mater. Sci. Eng.: A 790 (2020) 139704, https://doi.org/10.1016/j.msea.2020.139704.
[8] K. Wang, D. Du, G. Liu, Z. Pu, B. Chang, J. Ju, A study on the additive manufacturing of a high chromium Nickel-based superalloy by extreme high-speed laser metal deposition, Opt. Laser Technol. 133 (2021) 106504, https://doi.org/10.1016/j.optlastec.2020.106504.
[9] A. Marucco, Atomic ordering and α′-Cr phase precipitation in long-term aged Ni3Cr and Ni2Cr alloys, J. Mater. Sci. 30 (1995) 4188–4194, https://doi.org/10.1007/BF00360729.
[10] V.N. Gadalov, S.B. Maslenkov, A.S. Nagin, A.V. Petridis, Effect of atomic ordering on structure formation for a nickel alloy with high chromium content, Met Sci. Heat. Treat. 27 (1985) 522–524, https://doi.org/10.1007/BF00699584.
[11] X. Zhong, E.-H. Han, X. Wu, Corrosion behavior of Alloy 690 in aerated supercritical water, Corros. Sci. 66 (2013) 369–379, https://doi.org/10.1016/j.corsci.2012.10.001.

[12] U.C. Kim, K.M. Kim, E.H. Lee, Effects of chemical compounds on the stress corrosion cracking of steam generator tubing materials in a caustic solution, J. Nucl. Mater. 341 (2005) 169–174, https://doi.org/10.1016/j.jnucmat.2005.01.018.

[13] D.-J. Kim, H.P. Kim, S.S. Hwang, Susceptibility of Alloy 690 to stress corrosion cracking in caustic aqueous solutions, Nucl. Eng. Technol. 45 (2013) 67–72, https://doi.org/10.5516/NET.07.2012.021.

[14] Z. Bi, J. Dong, L. Zheng, X. Xie, Phenomenon and mechanism of high temperature low plasticity in high-Cr nickel-based superalloy, J. Mater. Sci. Technol. 29 (2013) 187–192, https://doi.org/10.1016/j.jmst.2012.12.010.

[15] Q. Ju, H. Ma, X. Fu, M. Wang, Hot deformation behavior of cast and homogenized Ni-35Cr based superalloy, Rare Met. Mater. Eng. 41 (2012) 310–314.

[16] L. Zheng, C. Xiao, G. Zhang, B. Han, D. Tang, Primary α phase and its effect on the impact ductility of a high Cr content cast Ni-base superalloy, J. Alloy. Compd. 527 (2012) 176–183, https://doi.org/10.1016/j.jallcom.2012.02.166.

[17] K. Wang, D. Du, G. Liu, Z. Pu, B. Chang, J. Ju, Microstructure and mechanical properties of high chromium nickel-based superalloy fabricated by laser metal deposition, Mater. Sci. Eng.: A 780 (2020) 139185, https://doi.org/10.1016/j.msea.2020.139185.

[18] C. Schlereth, C. Oskay, H. Hattendorf, B. Nowak, M.C. Galetz, Influence of Al and Fe additions on metal dusting of NiCr alloys, Mater. Corros. 73 (2022) 1346–1358, https://doi.org/10.1002/maco.202112935.

[19] B. Li, B. Gleeson, W.-T. Chen, H. Hattendorf, 2020, Effects of Minor Alloying Elements on the Metal-Dusting Behavior of Ni-Based Alloys, in: 2020: p. NACE-2020-14657.

[20] H. Hattendorf, J. Kloewer, 2018, Alloy 699 XA - A New Alloy for Application Under Metal Dusting Conditions, in: 2018: p. NACE-2018-11200.

[21] N. Kwabena Adomako, N. Haghdadi, S. Primig, Electron and laser-based additive manufacturing of Ni-based superalloys: a review of heterogeneities in microstructure and mechanical properties, Mater. Des. 223 (2022) 111245, https://doi.org/10.1016/j.matdes.2022.111245.

[22] Y. Kok, X.P. Tan, P. Wang, M.L.S. Nai, N.H. Loh, E. Liu, S.B. Tor, Anisotropy and heterogeneity of microstructure and mechanical properties in metal additive manufacturing: a critical review, Mater. Des. 139 (2018) 565–586, https://doi.org/10.1016/j.matdes.2017.11.021.

[23] X. Tan, Y. Kok, W.Q. Toh, Y.J. Tan, M. Descoins, D. Mangelinck, S.B. Tor, K. F. Leong, C.K. Chua, Revealing martensitic transformation and α/β interface evolution in electron beam melting three-dimensional-printed Ti-6Al-4V, Sci. Rep. 6 (2016) 26039, https://doi.org/10.1038/srep26039.

[24] X. Tan, Y. Kok, Y.J. Tan, M. Descoins, D. Mangelinck, S.B. Tor, K.F. Leong, C. K. Chua, Graded microstructure and mechanical properties of additive manufactured Ti–6Al–4V via electron beam melting, Acta Mater. 97 (2015) 1–16, https://doi.org/10.1016/j.actamat.2015.06.036.

[25] S.-H. Sun, Y. Koizumi, S. Kurosu, Y.-P. Li, A. Chiba, Phase and grain size inhomogeneity and their influences on creep behavior of Co–Cr–Mo alloy additive manufactured by electron beam melting, Acta Mater. 86 (2015) 305–318, https://doi.org/10.1016/j.actamat.2014.11.012.

[26] K. Kunze, T. Etter, J. Grässlin, V. Shklover, Texture, anisotropy in microstructure and mechanical properties of IN738LC alloy processed by selective laser melting (SLM), Mater. Sci. Eng.: A 620 (2015) 213–222, https://doi.org/10.1016/j.msea.2014.10.003.

[27] Y.-L. Kuo, S. Horikawa, K. Kakehi, Effects of build direction and heat treatment on creep properties of Ni-base superalloy built up by additive manufacturing, Scr. Mater. 129 (2017) 74–78, https://doi.org/10.1016/j.scriptamat.2016.10.035.

[28] T.D. McLouth, D.B. Witkin, G.E. Bean, S.D. Sitzman, P.M. Adams, J.R. Lohser, J.-M. Yang, R.J. Zaldivar, Variations in ambient and elevated temperature mechanical behavior of IN718 manufactured by selective laser melting via process parameter control, Mater. Sci. Eng.: A 780 (2020) 139184, https://doi.org/10.1016/j.msea.2020.139184.

[29] S. Wu, H.Y. Song, H.Z. Peng, P.D. Hodgson, H. Wang, X.H. Wu, Y.M. Zhu, M. C. Lam, A.J. Huang, A microstructure-based creep model for additively manufactured nickel-based superalloys, Acta Mater. 224 (2022) 117528, https://doi.org/10.1016/j.actamat.2021.117528.

[30] S. Wu, H.Z. Peng, X. Gao, P.D. Hodgson, H.Y. Song, Y.M. Zhu, Y. Tian, A.J. Huang, Improving creep property of additively manufactured Inconel 718 through specifically-designed post heat treatments, Mater. Sci. Eng.: A 857 (2022) 144047, https://doi.org/10.1016/j.msea.2022.144047.

[31] G. Lindwall, C.E. Campbell, E.A. Lass, F. Zhang, M.R. Stoudt, A.J. Allen, L. E. Levine, Simulation of TTT curves for additively manufactured inconel 625, Met. Mater. Trans. A 50 (2019) 457–467, https://doi.org/10.1007/s11661-018-4959-7.

[32] A. Mostafaei, R. Ghiaasiaan, I.-T. Ho, S. Strayer, K.-C. Chang, N. Shamsaei, S. Shao, S. Paul, A.-C. Yeh, S. Tin, A.C. To, Additive manufacturing of nickel-based superalloys: a state-of-the-art review on process-structure-defect-property relationship, Prog. Mater. Sci. 136 (2023) 101108, https://doi.org/10.1016/j.pmatsci.2023.101108.

[33] K.-T. Son, T.Q. Phan, L.E. Levine, K.-S. Kim, K.-A. Lee, M. Ahlfors, M.E. Kassner, The creep and fracture properties of additively manufactured inconel 625, Materialia 15 (2021) 101021, https://doi.org/10.1016/j.mtla.2021.101021.

[34] J. Xu, H. Gruber, D. Deng, R.L. Peng, J.J. Moverare, Short-term creep behavior of an additive manufactured non-weldable Nickel-base superalloy evaluated by slow strain rate testing, Acta Mater. 179 (2019) 142–157, https://doi.org/10.1016/j.actamat.2019.08.034.

[35] H. Hilal, R. Lancaster, S. Jeffs, J. Boswell, D. Stapleton, G. Baxter, The influence of process parameters and build orientation on the creep behaviour of a laser powder bed fused Ni-based superalloy for aerospace applications, Materials 12 (2019) 1390, https://doi.org/10.3390/ma12091390.

[36] S. Jeffs, R.J. Lancaster, S. Davies, Effect of build orientation and post processing of a direct laser deposited nickel superalloy as determined by the small punch creep test, Key Eng. Mater. 734 (2017) 128–136, https://doi.org/10.4028/www.scientific.net/KEM.734.128.

[37] S.J. Davies, S.P. Jeffs, M.P. Coleman, R.J. Lancaster, Effects of heat treatment on microstructure and creep properties of a laser powder bed fused nickel superalloy, Mater. Des. 159 (2018) 39–46, https://doi.org/10.1016/j.matdes.2018.08.039.

[38] E. De Bruycker, A. Gotti, E. Poggio, K. Boschmans, O. Tassa, A. Costa, A. Sanguineti, Short-term creep behaviour of additive manufactured Hastelloy X material, Mater. High. Temp. 39 (2022) 462–471, https://doi.org/10.1080/09603409.2022.2041849.

[39] C.M.F. Rae, R.C. Reed, Primary creep in single crystal superalloys: Origins, mechanisms and effects, Acta Mater. 55 (2007) 1067–1081, https://doi.org/10.1016/j.actamat.2006.09.026.

[40] T.M. Pollock, A.S. Argon, Creep resistance of CMSX-3 nickel base superalloy single crystals, Acta Metall. Et. Mater. 40 (1992) 1–30, https://doi.org/10.1016/0956-7151(92)90195-K.

[41] J. Svoboda, P. Lukáš, Creep deformation modelling of superalloy single crystals, Acta Mater. 48 (2000) 2519–2528, https://doi.org/10.1016/S1359-6454(00)00078-1.

[42] P.R. Bhowal, E.F. Wright, E.L. Raymond, Effects of cooling rate and γ′ morphology on creep and stress-rupture properties of a powder metallurgy superalloy, Met. Trans. A 21 (1990) 1709–1717, https://doi.org/10.1007/BF02672587.

[43] S. Raujol, M. Benyoucef, D. Locq, P. Caron, F. Pettinari, N. Clement, A. Coujou, Decorrelated movements of Shockley partial dislocations in the γ-phase channels of nickel-based superalloys at intermediate temperature, Philos. Mag. 86 (2006) 1189–1200, https://doi.org/10.1080/14786430500254685.

[44] F. Bachmann, R. Hielscher, H. Schaeben, Grain detection from 2d and 3d EBSD data—Specification of the MTEX algorithm, Ultramicroscopy 111 (2011) 1720–1733, https://doi.org/10.1016/j.ultramic.2011.08.002.

[45] G. Nolze, R. Hielscher, Orientations – perfectly colored, J. Appl. Cryst. 49 (2016) 1786–1802, https://doi.org/10.1107/S1600576716012942.

[46] D.G. Brandon, The structure of high-angle grain boundaries, Acta Metall. 14 (1966) 1479–1484, https://doi.org/10.1016/0001-6160(66)90168-4.

[47] A. Ayad, M. Ramoul, A.D. Rollett, F. Wagner, Quantifying primary recrystallization from EBSD maps of partially recrystallized states of an IF steel, Mater. Charact. 171 (2021) 110773, https://doi.org/10.1016/j.matchar.2020.110773.

[48] C. Haase, L.A. Barrales-Mora, F. Roters, D.A. Molodov, G. Gottstein, Applying the texture analysis for optimizing thermomechanical treatment of high manganese twinning-induced plasticity steel, Acta Mater. 80 (2014) 327–340, https://doi.org/10.1016/j.actamat.2014.07.068.

[49] J. Xu, H. Gruber, D. Deng, R.L. Peng, J.J. Moverare, Short-term creep behavior of an additive manufactured non-weldable Nickel-base superalloy evaluated by slow strain rate testing, Acta Mater. 179 (2019) 142–157, https://doi.org/10.1016/j.actamat.2019.08.034.

[50] https://www.jems-swiss.ch/Home/jemsWebSite/Introduction.html.

[51] C.A. Schneider, W.S. Rasband, K.W. Eliceiri, NIH Image to ImageJ: 25 years of image analysis, Nat. Methods 9 (2012) 671–675, https://doi.org/10.1038/nmeth.2089.

[52] A.P. Hammersley, S.O. Svensson, M. Hanfland, A.N. Fitch, D. Hausermann, Two-dimensional detector software: From real detector to idealised image or two-theta scan, High. Press. Res. 14 (1996) 235–248, https://doi.org/10.1080/08957959608201408.

[53] A.P. Hammersley, FIT2D: an introduction and overview. ESRF Internal Report ESRF97HA02T, European Synchrotron Radiation Source, Grenoble, France, 1997.

[54] M. Ferrari, L. Lutterotti, Method for the simultaneous determination of anisotropic residual stresses and texture by x-ray diffraction, J. Appl. Phys. 76 (1994) 7246–7255, https://doi.org/10.1063/1.358006.

[55] T. Hostinský, J. Čadek, A constant tensile stress creep testing machine, J. Test. Eval. 4 (1976) 26–28, https://doi.org/10.1520/JTE10503J.

[56] J. Pešička, R. Kužel, A. Dronhofer, G. Eggeler, The evolution of dislocation density during heat treatment and creep of tempered martensite ferritic steels, Acta Mater. 51 (2003) 4847–4862, https://doi.org/10.1016/S1359-6454(03)00324-0.

[57] J. Fu, Q. Nie, W. Qiu, J. Liu, Y. Wu, Morphology, orientation relationships and formation mechanism of TiN in Fe-17Cr steel during solidification, Mater. Charact. 133 (2017) 176–184, https://doi.org/10.1016/j.matchar.2017.10.001.

[58] A. Durga, N.H. Pettersson, S.B.A. Malladi, Z. Chen, S. Guo, L. Nyborg, G. Lindwall, Grain refinement in additively manufactured ferritic stainless steel by in situ inoculation using pre-alloyed powder, Scr. Mater. 194 (2021) 113690, https://doi.org/10.1016/j.scriptamat.2020.113690.

[59] A. Després, C. Mayer, M. Veron, E.F. Rauch, M. Bugnet, J.-J. Blandin, G. Renou, C. Tassin, P. Donnadieu, G. Martin, On the variety and formation sequence of second-phase particles in nickel-based superalloys fabricated by laser powder bed fusion, Materialia 15 (2021) 101037, https://doi.org/10.1016/j.mtla.2021.101037.

[60] A. Després, S. Antonov, C. Mayer, M. Veron, E.F. Rauch, C. Tassin, J.-J. Blandin, P. Kontis, G. Martin, Revealing the true partitioning character of zirconium in additively manufactured polycrystalline superalloys, Addit. Manuf. Lett. 1 (2021) 100011, https://doi.org/10.1016/j.addlet.2021.100011.

[61] H. Yu, S. Hayashi, K. Kakehi, Y.-L. Kuo, Study of formed oxides in IN718 alloy during the fabrication by selective laser melting and electron beam melting, Metals 9 (2019) 19, https://doi.org/10.3390/met9010019.

[62] M. Cloots, P.J. Uggowitzer, K. Wegener, Investigations on the microstructure and crack formation of IN738LC samples processed by selective laser melting using Gaussian and doughnut profiles, Mater. Des. 89 (2016) 770–784, https://doi.org/10.1016/j.matdes.2015.10.027.

[63] A. Hariharan, L. Lu, J. Risse, A. Kostka, B. Gault, E.A. Jägle, D. Raabe, Misorientation-dependent solute enrichment at interfaces and its contribution to defect formation mechanisms during laser additive manufacturing of superalloys, Phys. Rev. Mater. 3 (2019) 123602, https://doi.org/10.1103/PhysRevMaterials.3.123602.
[64] V.P.N. Samy, F. Brasche, F. Yan, I. Šulák, B. Bezci, B. Nowak, I. Berglund, U. Krupp, C. Haase, Understanding the High-Temperature Deformation Behavior of Additively Manufactured γ'-forming Ni-based alloys by Microstructure Heterogeneities-Integrated Creep Modelling, Addit. Manuf. (2024) 104256, https://doi.org/10.1016/j.addma.2024.104256.
[65] M. Duan, G. Bai, S. Guo, Y. Peng, X. Liu, W. Zhang, X. Zhang, Y. Huang, J. Liu, G. Gao, J. Kong, Q. Zhou, K. Wang, Dynamic tensile mechanical properties of 18Ni350 maraging steel fabricated by wire arc additive manufacturing, J. Mater. Res. Technol. 25 (2023) 5426–5442, https://doi.org/10.1016/j.jmrt.2023.06.276.
[66] K. Saravanan, V.S.K. Chakravadhanula, S.K. Manwatkar, S.V.S. Narayana Murty, P. Ramesh Narayanan, Dynamic strain aging and embrittlement behavior of IN718 during high-temperature deformation, Met. Mater. Trans. A 51 (2020) 5691–5703, https://doi.org/10.1007/s11661-020-05970-3.
[67] F.C. Monkman, N.J. Grant, An empirical relationship between rupture life and minimum creep rate in creep rupture tests, Proc. ASTM Int. 28 (1956) 593–620. ⟨https://www.astm.org/DIGITAL_LIBRARY/STP/MMR/PAGES/PRO1956-56.html⟩.
[68] F.R. Larson, J. Miller, A time-temperature relationship for rupture and creep stresses, Trans. Am. Soc. Mech. Eng. 74 (2022) 765–771, https://doi.org/10.1115/1.4015909.
[69] V. Sklenička, K. Kuchařová, M. Svoboda, M. Kvapilová, P. Král, J. Dvořák, Creep behaviour of IN 740 alloy after HAZ thermal cycle simulations, Int. J. Press. Vessels Pip. 178 (2019) 104000, https://doi.org/10.1016/j.ijpvp.2019.104000.
[70] M.E. Kassner, Chapter 10 - Creep Fracture, in: M.E. Kassner (Ed.), Fundamentals of Creep in Metals and Alloys (Third Edition), Butterworth-Heinemann, Boston, 2015, pp. 233–260, https://doi.org/10.1016/B978-0-08-099427-7.00010-4.
[71] T.-H. Lee, H.-Y. Suh, S.-K. Han, J.-S. Noh, J.-H. Lee, Effect of a heat treatment on the precipitation behavior and tensile properties of alloy 690 steam generator tubes, J. Nucl. Mater. 479 (2016) 85–92, https://doi.org/10.1016/j.jnucmat.2016.06.038.
[72] W. Wang, S. Lartigue-Korinek, F. Brisset, A.L. Helbert, J. Bourgon, T. Baudin, Formation of annealing twins during primary recrystallization of two low stacking fault energy Ni-based alloys, J. Mater. Sci. 50 (2015) 2167–2177, https://doi.org/10.1007/s10853-014-8780-4.
[73] L. Wang, G. Xie, J. Zhang, L.H. Lou, On the role of carbides during the recrystallization of a directionally solidified nickel-base superalloy, Scr. Mater. 55 (2006) 457–460, https://doi.org/10.1016/j.scriptamat.2006.05.013.
[74] M.J. Donachie, S.J. Donachie, Superalloys: A Technical Guide, 2nd Edition, ASM International, 2002.
[75] S. Kihara, J.B. Newkirk, A. Ohtomo, Y. Saiga, Morphological changes of carbides during creep and their effects on the creep properties of inconel 617 at 1000 °C, Met. Trans. A 11 (1980) 1019–1031, https://doi.org/10.1007/BF02654716.
[76] J.B. Singh, A. Verma, B. Paul, J.K. Chakravartty, Failure of alloy 625 tube stub ends – effect of primary nitrides, Eng. Fail. Anal. 32 (2013) 236–247, https://doi.org/10.1016/j.engfailanal.2013.03.018.
[77] G. Bi, G.K.L. Ng, K.M. Teh, A.E.W. Jarfors, Feasibility study on the laser aided additive manufacturing of die inserts for liquid forging, Mater. Des. 31 (2010) S112–S116, https://doi.org/10.1016/j.matdes.2009.10.039.
[78] K. Liu, J. Wang, Y. Yang, Y. Zhou, Effect of cooling rate on carbides in directionally solidified nickel-based single crystal superalloy: X-ray tomography and U-net CNN quantification, J. Alloy. Compd. 883 (2021) 160723, https://doi.org/10.1016/j.jallcom.2021.160723.
[79] W.L. Grube, S.R. Rouze, The origin, growth and annihilation of annealing twins in austenite, Can. Metall. Q. 2 (1963) 31–52, https://doi.org/10.1179/cmq.1963.2.1.31.
[80] O.M.D.M. Messé, R. Muñoz-Moreno, T. Illston, S. Baker, H.J. Stone, Metastable carbides and their impact on recrystallisation in IN738LC processed by selective laser melting, Addit. Manuf. 22 (2018) 394–404, https://doi.org/10.1016/j.addma.2018.05.030.
[81] K. Sourabh, J.B. Singh, Creep behaviour of alloy 690 in the temperature range 800–1000 °C, J. Mater. Res. Technol. 17 (2022) 1553–1569, https://doi.org/10.1016/j.jmrt.2022.01.060.
[82] M. Ivanchenko, V. Nevdacha, Y. Yagodzinskyy, H. Hänninen, Internal friction studies of carbon and its redistribution kinetics in Inconel 600 and 690 alloys under dynamic strain aging conditions, Mater. Sci. Eng.: A 442 (2006) 458–461, https://doi.org/10.1016/j.msea.2006.02.207.
[83] T.E. Moss, G.S. Was, Dynamic strain aging of nickel-base alloys 800H and 690, Met. Mater. Trans. A 43 (2012) 3428–3432, https://doi.org/10.1007/s11661-012-1335-x.
[84] J. Risse, Additive manufacturing of nickel-base superalloy IN738LC by laser powder bed fusion (Ph.D. thesis), RWTH Aachen (2019) 190–195, https://doi.org/10.18154/RWTH-, 2019- 06822.
[85] K.L. Murty, S. Gollapudi, K. Ramaswamy, M.D. Mathew, I. Charit, Creep deformation of materials in light water reactors (LWRs). Materials Ageing and Degradation in Light Water Reactors, Elsevier, 2013, pp. 81–148, https://doi.org/10.1533/9780857097453.1.81.
[86] A. Manonukul, F.P.E. Dunne, D. Knowles, Physically-based model for creep in nickel-base superalloy C263 both above and below the gamma solvus, Acta Mater. 50 (2002) 2917–2931, https://doi.org/10.1016/S1359-6454(02)00119-2.
[87] L. Thébaud, P. Villechaise, J. Cormier, C. Crozet, A. Devaux, D. Béchet, J.-M. Franchet, A. Organista, F. Hamon, Relationships between microstructural parameters and time-dependent mechanical properties of a new nickel-based superalloy AD730™, Metals 5 (2015) 2236–2251, https://doi.org/10.3390/met5042236.
[88] Y. Zhao, K. Li, M. Gargani, W. Xiong, A comparative analysis of inconel 718 made by additive manufacturing and suction casting: Microstructure evolution in homogenization, Addit. Manuf. 36 (2020) 101404, https://doi.org/10.1016/j.addma.2020.101404.
[89] Y.S. Lim, J.S. Kim, H.P. Kim, H.D. Cho, The effect of grain boundary misorientation on the intergranular M23C6 carbide precipitation in thermally treated alloy 690, J. Nucl. Mater. 335 (2004) 108–114, https://doi.org/10.1016/j.jnucmat.2004.07.038.
[90] D. Spader, K. Maciejewski, H. Ghonem, Distribution of grain boundary carbides in inconel 617 subjected to creep at 900 °C and 950 °C, Met. Mater. Trans. A 51 (2020) 3473–3487, https://doi.org/10.1007/s11661-020-05798-x.
[91] S. Schlegel, S. Hopkins, E. Young, J. Cole, T. Lillo, M. Frary, Precipitate redistribution during creep of alloy 617, Met. Mater. Trans. A 40 (2009) 2812–2823, https://doi.org/10.1007/s11661-009-0027-7.
[92] S. Xu, A.K. Koul, J.I. Dickson, Creep crack growth in the absence of grain boundary precipitates in UDIMET 520, Met. Mater. Trans. A 32 (2001) 795–804, https://doi.org/10.1007/s11661-001-0095-9.
[93] T. Hentrich, H. Hattendorf, S. Bellmann, B. Nowak, 2023, Investigations on the Microstructural Stability After Long-Term High-Temperature Exposure of Alloy 699 XA, in: 2023: p. AMPP-2023-18845.
[94] M. Detrois, K.A. Rozman, P.D. Jablonski, J.A. Hawk, An alternative casting technique to improve the creep resistance of cast INCONEL alloy 740H, Met. Mater. Trans. A 51 (2020) 3819–3831, https://doi.org/10.1007/s11661-020-05822-0.
[95] E. El-Magd, G. Nicolini, M. Farag, Effect of carbide precipitation on the creep behavior of alloy 800HT in the temperature range 700 ° to 900 °, Met. Mater. Trans. A 27 (1996) 747–756, https://doi.org/10.1007/BF02648962.
[96] Q. Li, S. Tian, H. Yu, N. Tian, Y. Su, Y. Li, Effects of carbides and its evolution on creep properties of a directionally solidified nickel-based superalloy, Mater. Sci. Eng.: A 633 (2015) 20–27, https://doi.org/10.1016/j.msea.2015.02.056.